Icarus 202 (2009) 160–180

Contents lists available at ScienceDirect

Icarus

www.elsevier.com/locate/icarus

An extension of the Bus asteroid taxonomy into the near-infrared

Francesca E. DeMeo [a,*], Richard P. Binzel [b], Stephen M. Slivan [b], Schelte J. Bus [c]

[a] LESIA, Observatoire de Paris, F-92195 Meudon Principal Cedex, France
[b] Department of Earth, Atmospheric, and Planetary Sciences, Massachusetts Institute of Technology, Cambridge, MA 02139, United States
[c] Institute for Astronomy, 640 N. Aohoku Place, Hilo, HI 96720, United States

ARTICLE INFO

Article history:
Received 30 October 2008
Revised 6 February 2009
Accepted 9 February 2009
Available online 14 February 2009

Keywords:
Asteroids
Spectroscopy

ABSTRACT

The availability of asteroid spectral measurements extending to the near-infrared, resulting from the development of new telescopic instruments (such as SpeX [Rayner, J.T., and 7 colleagues, 2003. Astron. Soc. Pacific 115, 362–382]), provides a new basis for classifying asteroid reflectance spectra. We present an asteroid taxonomy classification system based on reflectance spectrum characteristics for 371 asteroids measured over the wavelength range 0.45 to 2.45 μm. This system of 24 classes is constructed using principal component analysis, following most closely the visible wavelength taxonomy of Bus [Bus, S.J., 1999. Ph.D. thesis, Massachusetts Institute of Technology], which itself builds upon the system of Tholen [Tholen, D.J., 1984. Ph.D. thesis, University of Arizona]. Nearly all of the Bus taxonomy classes are preserved, with one new class (Sv) defined. For each class we present boundary definitions, spectral descriptions, and prototype examples. A flow chart method is presented for classifying newly acquired data spanning this wavelength range. When data are available only in the near-infrared range (0.85 to 2.45 μm), classification is also possible in many cases through an alternate flow chart process. Within our sample, several classes remain relatively rare: only 6 objects fall into the A-class; 349 Dembowska and 3628 Boznemcova reside as the only objects in their respective R- and O-classes. Eight Q-class objects are all near-Earth asteroids. We note 1904 Massevitch as an outer main-belt V-type while 15 other V-type objects have inner main-belt orbits consistent with an association with Vesta.

1. Introduction

Taxonomic classification systems for asteroids have existed since there were enough data to distinguish meaningful groups. The first taxonomies were based on asteroid broad band filter colors such as Wood and Kuiper (1963) and Chapman et al. (1971) where they noted two separate types of objects denoted as "S" and "C". Taxonomies and their nomenclature grew and evolved as later taxonomies became based on higher resolution spectral data which reveal features offering clues to surface composition, age, and alteration. The most widely used taxonomies for asteroids currently are the Tholen taxonomy (1984) based on the Eight-Color Asteroid Survey data (ECAS, Zellner et al., 1985) and SMASSII spectral taxonomy (Bus, 1999; Bus and Binzel, 2002a, 2002b) based on the SMASSII spectral dataset. For a review of the evolution of asteroid taxonomies see Bus (1999).

Both the Tholen and Bus taxonomies were based on Principal Component Analysis, a dimension-reducing technique first applied to the field of asteroid classification by Tholen (1984). Most previous asteroid taxonomies were based on visible data because only in the current decade has spectral data collection become widely available in the near-infrared for asteroids down to relatively faint ($V = 17$) limiting magnitudes. The instrument SpeX on the NASA Infrared Telescope Facility (IRTF) has been crucial to increasing the library of near-IR asteroid spectra (Rayner et al., 2003).

The near-IR data range reveals diagnostic compositional information because of the presence of features at 1 and 2 μm primarily due to the presence of olivine and pyroxene. Other classification systems created using near-IR data include Howell et al. (1994) who created a neural network taxonomy. Gaffey et al. (1993) created an S-complex taxonomy of olivine- and pyroxine-rich asteroids based on near-infrared data. Our goal was to create a taxonomy extending from visible to near-infrared wavelengths for the entire suite of asteroid characteristics with a method that can be easily reproduced by future users to classify new data. We also strove to keep the notation consistent with past taxonomies, specifically the Bus taxonomy, to facilitate the transition to this new system. The Bus taxonomy, in turn, strove to keep its notation consistent with the Tholen taxonomy.

The taxonomy we present here is based on Principal Component Analysis. It is comprised of 24 classes compared to 26 in the Bus system with three Bus classes eliminated (Sl, Sk, Ld) and one (Sv) created, as well as the addition of a "w" notation, a mark

* Corresponding author. Fax: +33 1 45 07 71 44.
E-mail address: francesca.demeo@obspm.fr (F.E. DeMeo).

0019-1035/$ – see front matter
doi:10.1016/j.icarus.2009.02.005

meant to flag objects having similar spectral features but differing only by having a higher spectral slope. In this paper we present the data involved in the taxonomy and the method and rationale for the class definitions. The taxonomy classes are formally defined by data spanning the wavelength range 0.45 to 2.45 μm as compared with 0.34 to 1.04 μm for Tholen (1984) using eight points, and 0.435 to 0.925 μm for Bus (1999) using 48 points. A method of interpreting near-infrared data from 0.85 to 2.45 microns is also described but for many classes IR-only data do not yield a unique outcome in Principal Component Analysis (PCA) and the data cannot formally be classified. There is also a web application that determines taxonomic types for visible plus near-infrared data or near-infrared-only data based on this extended taxonomy (http://smass.mit.edu/busdemeoclass.html).

2. The data

New data presented here are near-infrared spectral measurements from 0.8 to 2.5 μm obtained using SpeX, the low- to medium-resolution near-IR spectrograph and imager (Rayner et al., 2003), on the 3-meter NASA IRTF located on Mauna Kea, Hawaii. As described in DeMeo and Binzel (2008), objects and standard stars were observed near the meridian to minimize their differences in airmass and match their parallactic angle to the fixed N/S alignment of the slit. Frames were taken so that the object was alternated between two different positions (usually noted as the A and B positions) on a 0.8×15 arcsecond slit aligned north–south. The asteroid spectrum was divided by the spectrum of a solar-type star, giving relative reflectance. Our primary solar analog standard stars were 16 Cyg B and Hyades 64. Additional solar analog stars with comparable spectral characteristics were utilized around the sky. Two to three sets of eight spectra per set were taken for each object, with each with exposures typically being 120 s. The total integration time for each of these objects therefore ranged from 30 to 120 min.

Reduction was performed using a combination of routines within the Image Reduction and Analysis Facility (IRAF), provided by the National Optical Astronomy Observatories (NOAO) (Tody, 1993), and Interactive Data Language (IDL). We use a software tool called "autospex" to streamline reduction procedures. Autospex writes macros containing a set of IRAF (or IDL) command files that are then executed by the image processing package. Autospex procedures operate on a single night at a time, with the opportunity for the user to inspect and verify the results at each stage. Briefly, autospex writes macros that: trim the images down to their useful area, create a bad pixel map from flat field images, flat field correct all images, perform the sky subtraction between AB image pairs, register the spectra in both the wavelength and spatial dimensions, co-add the spectral images for individual objects, extract the 2D spectra from co-added images, and then apply the final wavelength calibration. Using IDL, an absorption coefficient based on the atmospheric transmission (ATRAN) model by Lord (1992) is determined for each object and star pair that best minimizes atmospheric water absorption effects for that pair. This coefficient correction is most important near 1.4 and 2.0 μm, locations of major absorption bands due to telluric H_2O. The final IDL step averages all the object and standard pairs to create the final reflectance spectrum for each object.

Most (321) visible wavelength spectra (usually 0.4 to 0.9 μm) were taken from the Small Main Belt Asteroid Spectroscopic Survey (SMASS II) data set (Bus and Binzel, 2002a). Our sample was comprised of 371 objects with both visible and near-IR data. For a table of observations and references for all data included in this work as well as the final taxonomic designations for all objects see Appendix A. The spectra are plotted in Appendix D.

3. Creating the taxonomy

Principal Component Analysis (PCA) is a method of reducing the dimensionality of a data set, involving coordinate transformations to minimize the variance. The first transformation rotates the data to maximize variance along the first axis, known as Principal Component 1 (PC1′), the second axis is the second Principal Component (PC2′). The first few principal components contain the majority of the information. For a more thorough explanation of PCA and why it is useful for asteroid taxonomy refer to Tholen (1984) and Bus (1999).

3.1. Data preparation

To prepare our data, we created "spline fits" to our spectra which smoothed the spectra creating a "best fit" curve. This reduced the risk that noise or missing data points would influence the resulting taxonomy. We sampled the region 0.45 to 2.45 μm and recorded values of the spline fit at increments of 0.05 μm resulting in 41 datapoints.

The "splined" data were then normalized at 0.55 μm and the slope was removed from the data and recorded. Using our normalized data, we took a linear regression line of each set of data. The slope (γ) of the linear regression line is defined by Eq. (1):

$$\gamma = \frac{\sum_0^i (x_i - \bar{x})(y_i - \bar{y})}{\sum_0^i (x_i - \bar{x})^2}, \tag{1}$$

where x_i is each wavelength value, y_i is each fitted reflectance, and $\bar{x}$ and $\bar{y}$ are their mean values. We note the slope is not constrained to pass through 1 at 0.55 μm. The calculated slope is thus independent of one's choice for the wavelength at which a spectrum is normalized. The equation of the line defining the slope is then translated in the y-direction to pass through 1 at 0.55 μm.

Because slope is the most prominent feature of the spectra we remove it from the data by dividing the slope function, before performing principal component analysis thus making PCA more sensitive to other features. We divide all the data points by the fitted slope. The remaining data are a spectrum with an average slope of zero residuals (including absorption features) above and below the horizontal. We now have data with 41 channels normalized to unity at 0.55 μm with the slope removed. Because each spectrum has a value of 1 at 0.55 μm, that channel provides no new information and so was removed from the data set to make PCA more effective. Therefore we input 40 channels per object into PCA. Using MATLAB, we then performed PCA on the splined files with slopes removed. We chose to use covariance instead of correlation for the PCA implementation as suggested by Bus (1999).

Following the method of Bus (1999), we verify the slope as a constant signal within all data. Fig. 1 displays the first principal component (PC1) of PCA before removing slope compared to the slope we remove directly from the splined data. In the figure it is clear that the two are linearly correlated, justifying the value of removing slope and tabulating it as a spectral parameter.

3.2. Notation

Here we offer a note on our notation: we use the "′" notation to denote that principal component analysis is performed on data from which the slope has been removed. Thus PC1′ is the first principal component of asteroid data that has already had its slope removed. To perform PCA the average value for each channel is subtracted from the data set, resulting in a data set with mean for each channel equal to zero. Note that this notation differs from the Bus (Bus, 1999; Bus and Binzel, 2002b) notation in which the

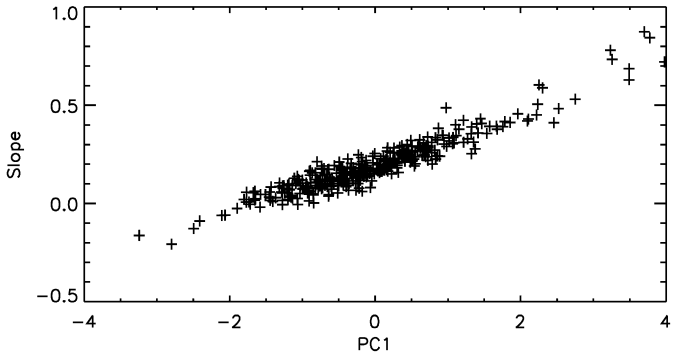

Fig. 1. Results for PC1 versus Slope. PC1 is the first principal component from a data set that did not have the slope removed. It is clear from the plot that PC1 and slope are linearly related and it is thus valid to remove the slope before running PCA to make PCA more sensitive to other features. Our treatment of slope as a tabulated and removed parameter follows the method of Bus (1999).

first principal component that has already had its slope removed is PC2′. The supplementary material provides a table of the eigenvalues for the first five principal components and the mean value for each channel. To compute the principal components of a data set, the transpose of the eigenvector is multiplied by the transpose of the mean-subtracted data set as described in Eq. (2):

$$\mathrm{PC}_x = \left[\mathrm{E}_x^T\right]\left[\mathrm{D}^T\right], \tag{2}$$

where PC_x is principal component x, E_x is eigenvector x. D is the column vector containing an individual reflectance spectrum, normalized to unity at 0.55 μm, from which the mean channel value (see supplementary material) has been subtracted at each wavelength.

3.3. Choosing the number of principal components

Bus (Bus, 1999; Bus and Binzel, 2002b) used slope plus two principal components to characterize visible data contained in 48 wavelength channels. Because 40 wavelength channels were put into our PCA, 40 principal components were the output. Since PCA concentrates the most information in the first dimensions, and decreases with each successive dimension, only the first few principal components are useful. To decide how many principal components to use in our analysis we look at the variance contained within each.

The first five principal components contain 99.2% of the variance, which is sufficient to describe these spectra. PC4′ and PC5′ were found to be useful for classifying the subtly featured X- and C-complex objects. To find the variance contained within the slope we ran PCA with the slope included in the data. Slope accounts for 88.4% of all the variance within the data. All the other principal components combined account for 11.6%. Thus, Slope plus the first five PC account for 99.9% of the variance. Table 1 shows the variances accounted for by the slope and each of the first five principal components.

Table 1
Variance of slope and principal components.

Principal component	Variance (%) (slope excluded)	Variance (%) (slope included)
Slope	–	88.4
PC1′	63.1	7.3
PC2′	24.3	2.8
PC3′	8.9	1.0
PC4′	2.2	0.3
PC5′	0.6	0.1
PC6′	0.3	0.1
PC7′	0.2	–
PC8′	0.1	–
PC9′	0.1	–
PC10′–PC40′	0.1	–
Total	100.0	100.0

4. The taxonomy

Of the 371 objects in our sample, 321 were previously assigned labels within the Bus taxonomy. We used this set of 321 objects to guide the class boundaries. The following describes the separation of complexes and classes and the resultant flow chart to reproduce these results using any dataset. Our method is similar to that of Bus (Bus, 1999; Bus and Binzel, 2002a, 2002b); we start by defining the end members, and then move to define the "core" of each complex. The three main complexes are consistent with past taxonomies: the S-complex displays strong absorptions at 1 and 2 μm, the C-complex shows low to medium slope and either small or no features, and the X-complex has medium to high slope also displays either small or no features. The complexes are meant to group classes that show similar characteristics. The end member classes are more distinct and separate farther from other types among their principal components. For all the new classifications of the 371 objects in our dataset see Appendix B.

4.1. The grand divide

The most striking feature seen within the principal component space is the large gap in PC1′ versus PC2′ space seen in Fig. 2. It appears that this clear boundary distinguishes between spectra that have a 2-μm absorption band and those that do not. This "grand divide" is well represented by Eq. (3):

$$\mathrm{PC1}' = -3.00\mathrm{PC2}' - 0.28 \quad (\text{line } \alpha). \tag{3}$$

This "grand divide" is a natural boundary revealed by the principal component analysis that relates PC1′ and PC2′. While no other boundary in this taxonomy is as distinct and well-defined, we used this natural divide as a guide for other, more artificially created boundaries. When defining classes to the right of line α, we used lines parallel and orthogonal to it to carve out the space. Figs. 2, 3 and 4 plot all objects in PC1′ and PC2′ space. Fig. 2 shows all objects. Fig. 3 shows only objects right of line α plus the A- and Sa-types with the boundaries and line labels that carve out this space. Fig. 4 shows objects left of line α except A- and Sa-types. It is clear from Fig. 4 that the C- and X-complexes do not separate clearly in this PC space. For plots showing the placement of objects in this sample with their Bus, Tholen, and Gaffey labels, see the supplementary material.

Except for some L-class objects at the top left of Fig. 2, all objects below and to the left of line α have no 2-μm absorption feature and include all subtly featured (C- and X-complex) spectra. By "subtly featured" we mean there may or may not be shallow absorption features particularly in the visible wavelength range, however, there are no prominent 1- or 2-μm absorption bands. Objects plotted to the right of and above the line have a 2-μm absorption feature. The only classes that cross this gap are the A- and Sa-classes. Interestingly the K-class, long considered as an intermediate between S and C, falls most squarely in the gap.

While there is no predefined key to understanding the significance of each principal component in separating different spectral types, looking at how the gradient of spectra is distributed in Fig. 2 helps us decipher what effect each principal component has. For objects to the right of line α, moving parallel to the line in the decreasing PC1′ direction corresponds to increasing 1-μm band depth and width. Moving perpendicular to the line in the increasing PC2′ direction (to the right) corresponds to increasing depth and width

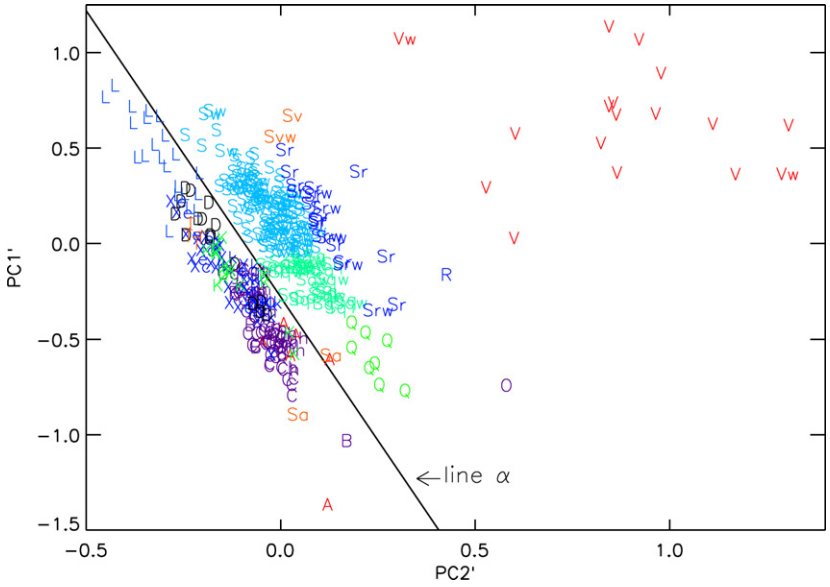

Fig. 2. Results for PC2′ versus PC1′. All objects plotted are labeled with their taxonomic classification in this system. Notice the "grand divide" between the S-complex and the C- and X-complexes. Line α separates objects with and without 2-μm absorption bands. The direction orthogonal to line α (increasing PC2′ values) indicates deeper 2-μm and narrower 1-μm absorption bands. The direction parallel to line α (increasing PC1′ values) indicates wider 1-μm absorption bands. The notation "PC1′", "PC2′", etc. denotes that these principal components are computed after removal of the slope.

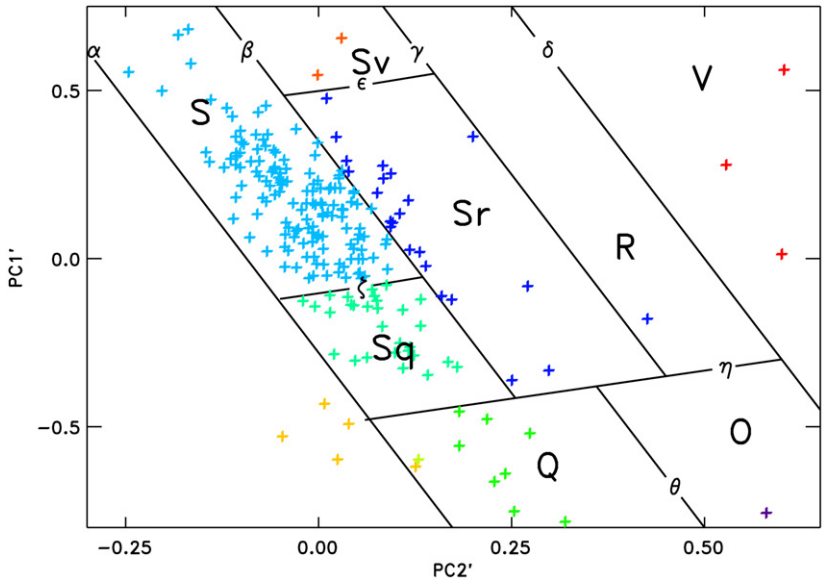

Fig. 3. PC2′ versus PC1′ plotted for the S-complex plus A-, Q-, O-, R-, and V-types. Boundaries chosen for each class are shown and lines are labeled with Greek letters. As described in the text, all boundaries are perpendicular or parallel to line α.

of the 2-μm band. The C- and X-complexes have subtler features, and thus have lower PC2′ values while S-complex objects have greater values and strongly featured end members such as V- and R-classes plot furthest to the right with the largest PC2′ values. As PC1′ values decrease (moving from top to bottom in Fig. 2) the 1-μm band becomes broader and in general deeper. The narrow 1-μm band V-types plot on the top right with wide Q- and even wider Sa- and A-types toward the bottom left. Types A, Q, and R with deeper bands all plot below the less extreme S-complex transition types, Sa, Sq, and Sr.

The guiding principle for the classification rules of this taxonomy was to define regions of principal component space that most consistently envelop objects within each of the original Bus (1999) classes. With this principle as a guide, we subjectively define boundaries so that the most similar spectra consistently fall into the same taxonomic classes. As discussed below, the overriding criterion of similarity of spectral properties in a class, as examined over the full 0.45–2.45 μm range, led to some objects in the Bus (Bus, 1999; Bus and Binzel, 2002b) classification receiving new class designations here.

To assign classes for the taxonomy we created a flowchart (Appendix B) containing steps to find a the taxonomic class that results in a consistent grouping of objects with similar spectral properties. The labels for each class follow, except where noted, the same label as Bus (Bus, 1999; Bus and Binzel, 2002b). The order of the flow chart is significant because some classes overlap in certain principal components but can be separated in others.

We start by separating the A- and Sa-classes because they cross over the "grand divide" in PC1′ and PC2′ space. This is step 1 in the flow chart. Refer to Appendix B for the complete chart. Spectrally, the A-class has a deep and extremely broad absorption band with

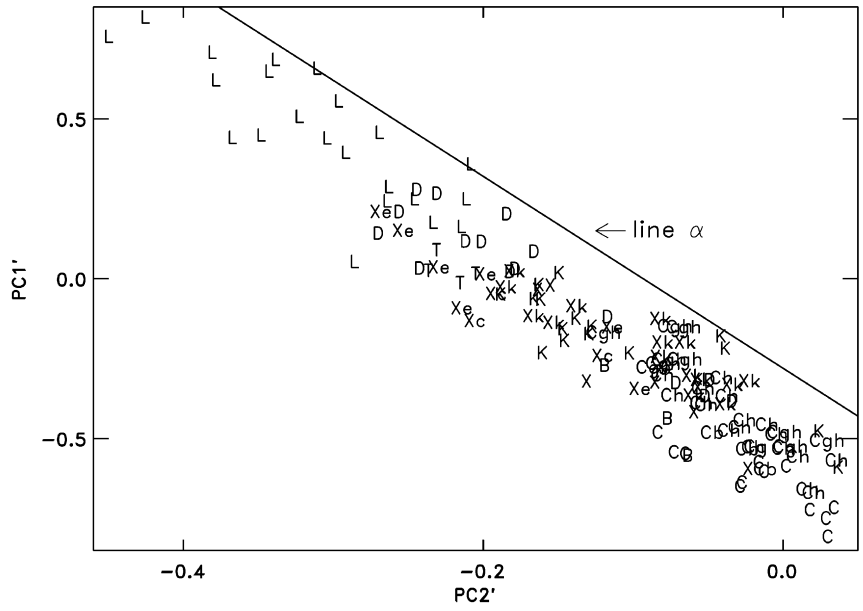

Fig. 4. PC2′ versus PC1′ plotted for the C- and X-complexes plus D-, K-, L-, and T-types. This principal component space does not clearly separate the classes.

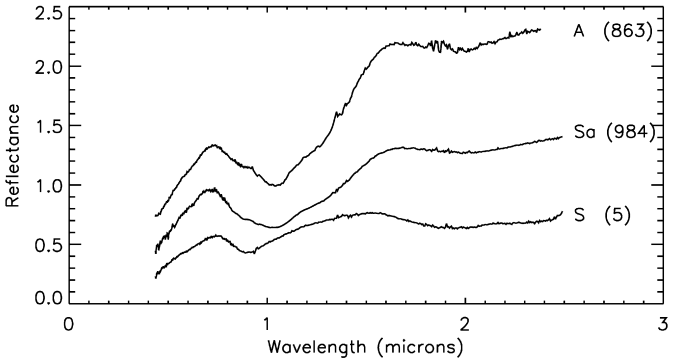

Fig. 5. Examples of S-, Sa-, and A-classes. There is a clear progression from S-types with a shallow 1-μm band and low slope to A-types with a deep 1-μm band and high slope. Sa- and A-types show similar 1-μm band absorptions, but Sa-types are much less red than A-types. The class and the asteroid number are labeled next to each spectrum.

a minimum near 1 μm and may or may not have shallow 2-μm absorption band; it also tends to be steeply sloped. The Sa-class has the same characteristic 1-μm absorption band as the A-class, but is less red.

The current Sa-class was redefined from the Bus system because the two Sa objects (main belt object 984 Gretia and Mars crosser 5261 Eureka) in this system were both Sr-types in the Bus system. Since these objects prove to be intermediate between S and A we change the classification of these two (Bus) Sr-types to Sa in this taxonomy. Fig. 5 shows the spectral progression from S to A.

Step two starts by separating all objects by the divide (line α) in PC2′ versus PC1′ space, and creates boundaries for objects with a 2-μm band. Step three addresses subtly featured objects (the C- and X-complexes) as well as the K-class which has no significant 2-μm band and the L-class which may or may not have a 2-μm absorption band but nonetheless lies to the left of line α.

4.2. The end members: O, Q, R, V

We started by looking at the end member classes in PCA space since they separate most clearly, thereby making them the easiest to define. In Fig. 3 one can see lines separating S-complex and end member classes. Equations (3), (4), (5), (6), and (7) bound these classes:

$$\mathrm{PC1}' = -3.0\mathrm{PC1}' + 1.5 \quad (\text{line } \delta), \tag{4}$$

$$\mathrm{PC1}' = -3.0\mathrm{PC1}' + 1.0 \quad (\text{line } \gamma), \tag{5}$$

$$\mathrm{PC1}' = \frac{1}{3}\mathrm{PC1}' - 0.5 \quad (\text{line } \eta), \tag{6}$$

$$\mathrm{PC1}' = -3.0\mathrm{PC1}' + 0.7 \quad (\text{line } \theta). \tag{7}$$

The V-class, based on the asteroid 4 Vesta (Tholen, 1984), is characterized by its strong and very narrow 1-μm absorption band, as well as a strong and wider 2-μm absorption feature. Most V-class asteroids that have been discovered are among the Vesta family and are known as Vestoids, although a few other objects have been identified throughout the main belt, such as 1459 Magnya (Lazzaro et al., 2000) and objects from the basaltic asteroid survey by Moskovitz et al. (2008). The R-class, created for its sole member 349 Dembowska by Tholen (1984), is similar to the V-class in that it displays deep 1- and 2-μm features, however the 1-μm feature is broader than the V-type feature and has a shape more similar to an S-type except with deeper features. The R-class region in principal component space is plotted in (Fig. 3). Bus (Bus and Binzel, 2002b) included three other members in the R-class, two of which are included in our sample. These two objects (1904 Massevitch and 5111 Jacliff) were reassigned to the V-class after discovering that in the near-infrared their 1-μm bands remain very narrow. Moskovitz et al. (2008) list 5111 Jacliff as an "R-type interloper" within the Vesta family, but it appears to be an object more confidently linked to Vesta. 1904 Massevitch, however, has a semi-major axis of 2.74 AU. The unusual spectrum and outer belt location for asteroid 1904 has been noted previously (e.g., Burbine and Binzel, 2002). In the sample we present here, asteroids 1904 Massevitch and 1459 Magnya (Lazzaro et al., 2000) are the only two V-types beyond 2.5 AU, a region where V-type asteroids are rare (Binzel et al., 2006, 2007; Moskovitz et al., 2008).

The O-class also has only one member, 3628 Boznemcova, defined by Binzel et al. (1993). Boznemcova is unique with a very rounded and deep, bowl shape absorption feature at 1-μm as well as a significant absorption feature at 2 μm. Even though the class

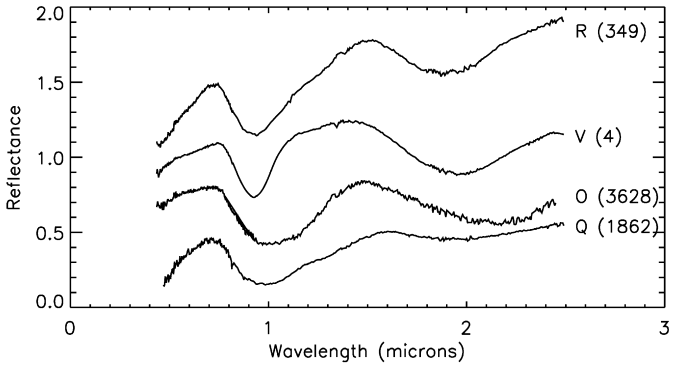

Fig. 6. Comparison of prototypes for the V-, O-, Q-, and R-classes. Note the O-class has a very wide 1-μm band and the V-class has a very narrow band. The V-types with the deepest 2-μm bands plot farthest from line α. For this and all subsequent spectral plots: We present relative reflectances normalized to unity at 0.55 μm; the spectra are offset vertically for clarity of comparison. The class and asteroid number are labeled next to each spectrum.

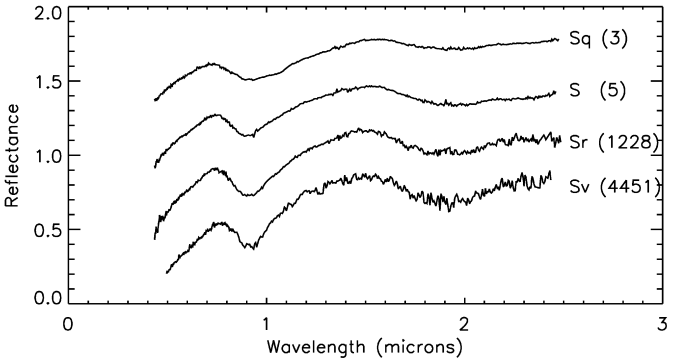

Fig. 7. Comparison of spectra within the S-complex (S, Sq, Sr, Sv) showing the variation in the 1-μm absorption band among these types. Sq-types have the widest 1-μm feature, similar to the Q-class. Sv-types have the narrowest feature, similar to the V-class.

is separated in the flow chart, more data on R-type and O-type objects may help establish more rigorously their region boundaries. Bus (Bus and Binzel, 2002b) designated three other asteroids as O-type, 4341 Poseiden, 5143 Heracles, and 1997 RT. Only 5143 was included in our sample. Asteroid 5143 is reclassified here as a Q-type because with near-infrared data it is clear the object did not have the distinct "bowl" shape of the 1-μm feature of Boznemcova. This adds 5143 Heracles as a Q-type to those known within near-Earth space (e.g., Binzel et al., 2004c).

The Q-class, whose boundaries are labeled in Fig. 3 was first defined by Tholen (1984) for near-Earth asteroid 1862 Apollo. The class is characterized by a deep and distinct 1-μm absorption feature with evidence of another feature near 1.3 μm as well as a 2-μm feature with varying depths among objects. The spectral differences between the end member classes V, R, Q, and O are displayed in Fig. 6.

4.3. The S-complex: S, Sa, Sq, Sr, Sv

Just as in the case of the Bus taxonomy, the S-complex was by far the most difficult to subdivide. Most Bus classes within the S-complex seemed to blend together or scatter randomly in all combinations of PCA components. For example, many objects labeled as "Sa" and "Sl" in the Bus (Bus, 1999; Bus and Binzel, 2002b) taxonomy no longer form distinct groups when their spectra are extended into the near-IR. Most original Bus class objects of these types merged into the S-class. Sa objects were most easily distinguishable not by absorption features, but by their greater slope (caused by slope increases in the 1- to 1.5-μm range). Similarly, many Bus S, Sq, and Sk objects become less clearly separated when their spectra extend to the near-infrared. Within PCA space, the Bus S, Sq, and Sk objects were initially impossible to define clearly because the boundaries blur and overlap. Because spectrally the main difference between the classes of the S-complex appears to be the width of the 1-μm absorption band we used the wavelength range 0.8 to 1.35 μm and performed PCA on only S-complex objects to gain insight on their differences.

Once we used this S-class PCA as a guide, it became more clear how to separate classes within PC1′ and PC2′. We continued to use boundaries parallel and perpendicular to line α. Each class has its own region in PC2′ and PC1′ space. Fig. 3 shows the S-complex boxes labeled in PCA space. The previously defined Eqs. (3), (5), (6), plus Eqs. (8), (9), and (10) bound the S-complex.

$$\mathrm{PC1}' = -3.0\mathrm{PC1}' + 0.35 \quad (\text{line } \beta), \tag{8}$$

$$\mathrm{PC1}' = \frac{1}{3}\mathrm{PC1}' - 0.10 \quad (\text{line } \zeta), \tag{9}$$

$$\mathrm{PC1}' = \frac{1}{3}\mathrm{PC1}' + 0.55 \quad (\text{line } \varepsilon). \tag{10}$$

Objects that reside just below the S-class in Fig. 3 appear similar to Q-types, but with more shallow absorption bands. These are Sq-types transitioning between S and Q. Sr-types transition between S- and R-classes. One object (5379 Abehiroshi) was a V-type under the Bus (Bus and Binzel, 2002b) system and is now labeled an Sr. While the visible data have a "moderate to very steep UV slope shortward of 0.7 μm with a sharp, extremely deep absorption band longward of 0.75 μm" (Bus and Binzel, 2002b), it is clear with the inclusion of near-infrared data that the 1-μm absorption band is too wide to be a V-type.

Two objects (2965 Surikov and 4451 Grieve) with high PC1′ values, are considered spectrally unique from Sr because they exhibit very narrow 1-μm absorption bands. The objects in this region spectrally appear to be in transition between S- and V-classes. They are not included in the Bus dataset, and Bus and Binzel (2002b) did not report any cases of objects with these characteristics. Because of their intermediate properties between S and V that are clearly displayed over the 0.45- to 2.45-μm range, we define a new class with the label Sv. Sk objects in the Bus taxonomy are found to become diverse when the spectra extend to near-IR wavelengths. All of these objects fall into other defined categories. Thus the Sk class is excluded from this new system. Fig. 7 displays the spectra of typical S-, Sq-, Sr-, and Sv-class spectra.

The objects in the S-complex had widely varying spectral slopes. To have some taxonomic distinction in spectral characteristics arising from slope, we made an arbitrary cutoff at slope = 0.25 dividing "high slope" objects from other objects. These objects are not relabeled in a class of their own. Instead the S, Sq, Sr, and Sv objects with high slopes receive a notation of "w" added to their name as a moniker for what is commonly discussed as an increase in slope arising from space weathering (Clark et al., 2002). [We make no pretense of knowing whether or not their surfaces are actually weathered.] The high slope S objects are labeled Sw, Sqw, Srw and Svw. We extended this flag to the V-types for which there were two objects with slopes greater than 0.25, which we label as Vw. Sa-types do not receive a w notation because, as an intermediate class between S and A, they are by definition highly sloped. Fig. 8 displays the differences between low- and high-slope objects, S and Sw.

The choice of 0.25 for the "w" notation is arbitrary. When plotting Bus labeled S, Sa, and Sl objects, there is a mixing around the 0.23 to 0.27 slope range. The goal was to keep the "w" notation more selective without setting the boundary too high where objects with unusual slope features (such as deeper UV dropoffs) were preferentially selected rather than focusing on the significant slope range between 1 and 2 μm for the S-complex. Fig. 9 plots

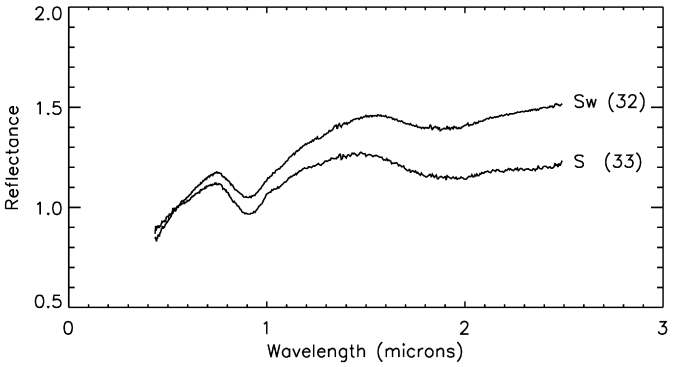

Fig. 8. Illustration of S and Sw reflectance spectra. The absorption features for both are very similar. Slope is the most significant distinction between the two, where the "w" is a notation to denote the slope difference, but does not describe a distinct class. These two spectra are not offset vertically, showing their differences relative to their common normalization at 0.55 μm.

Slope versus PC1′, showing the line separating "w" objects from regular objects.

4.4. The end members: D, K, L, T

Step three focuses on objects below or to the left of line α (Eq. (3)). We again start by removing end members. Bus (Bus and Binzel, 2002b) objects in the D- and T-classes continue to be easily separated by their high slopes and PC1′, PC2′, and PC3′ values. D-types have spectra that are linear with very steep slope (greater than 0.38), and some show slight curvature or a gentle kink around 1.5 μm. We note that some objects have their classification most strongly driven by their slope. It is possible for an object in the high-sloped A-class to fall very close to the A/D boundary (for example, the A-type 354 Eleonora). For objects near this boundary, a simple inspection for the presence of a 1-μm absorption band eliminates any possible confusion, where a strong 1-μm band is a distinctive feature of all A-types. T-types are linear with moderate to high slope (between 0.25 and 0.38) and often gently concaving down. We separate out L objects based on PC2′ versus PC1′. For objects residing in the L component space it is necessary to check for Xe-type objects. Xe is a class defined in the Bus system that is generally featureless except for a distinct hook at 0.49 μm, a feature that is not recognized within the first five components of PCA. By visually inspecting the spectrum, one can identify a feature at 0.49 and an absence of a slight feature around 1 μm and label the object as an Xe instead of an L. Refer to Fig. 10 of slope versus PC1′ which shows how D and L are fairly distinct. The K-types can then be distinguished clearly in PC2′ and PC3′ space.

The Bus (Bus and Binzel, 2002b) L- and K-classes were part of the S-class in the Tholen (1984) taxonomy. While the L-class may show 1- and 2-μm features, it is distinct from the S-class because the steep slope in visible region levels out abruptly around 0.7 μm, but does not show a distinct absorption band like the S. There is often a gentle concave down curvature in the near-infrared with a maximum around 1.5 μm, and there may or may not be a 2-μm absorption feature. A typical K-class object displays a wide absorption band centered just longward of 1 μm. This feature is unique because the left maximum and the minimum are sharply pointed and the walls of the absorption are linear with very little curvature. Fig. 11 plots typical spectra for the D-, L-, K-, T-, and X-classes.

We found that all Ld-type objects under the Bus system diverged into the separate L- and D-classes when near-infrared data were added. Thus the Ld-class itself is not necessary for distinguishing over the visible plus near-infrared wavelength range. The Ld-class does not continue into this new taxonomy.

4.5. The C- and X-complexes: B, C, Cb, Cg, Cgh, Ch; X, Xc, Xe, Xk

We now consider the core C- and X-complexes. The B-types are easily distinguished by their negative slope as well as negative PC1′ and PC4′ values. Their spectra are linear and negatively sloping often with a slight round bump around 0.6 μm preceding a slight feature longward of 1 μm and/or a slightly concave up curvature in the 1- to 2-μm region. The X-class can then be easily identified based on high slope values between 0.2 and 0.38. At this point Xe and Xk objects may be present in X-class PC space. Our PCA is not particularly sensitive to the small Xk feature, therefore the spectrum must be visually inspected for a slight feature present usually near 0.9 to 1 μm. If the feature is present, the object is designated an Xk. Xc-types have low to medium slope and are slightly curved and concave downward.

Ch objects have a small positive slope that begins around 1.1 μm and slightly pronounced UV dropoff, and a broad, shallow

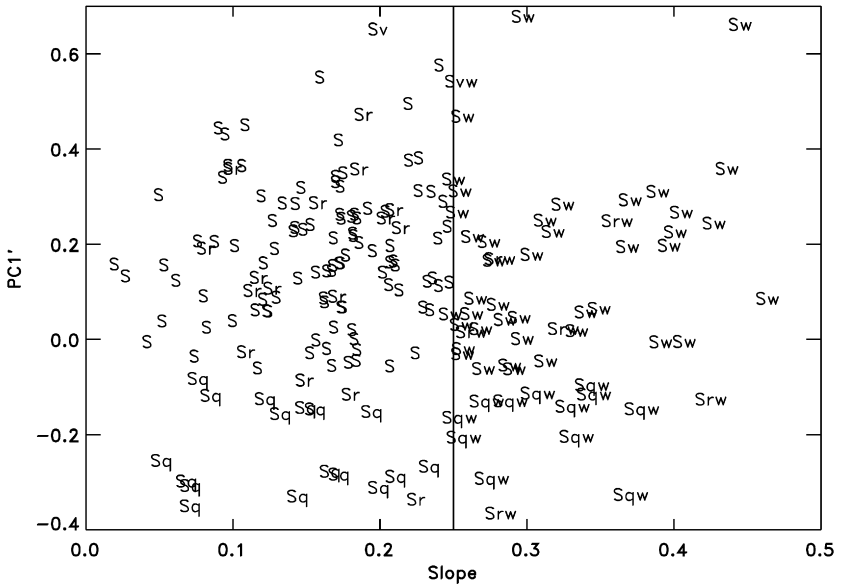

Fig. 9. Plot of slope versus PC1′ for the S-complex. All objects in classes S, Sq, Sr and Sv with slopes greater than 0.25 have a "w" notation to denote the high slope. This "w" notation not describe a distinct class.

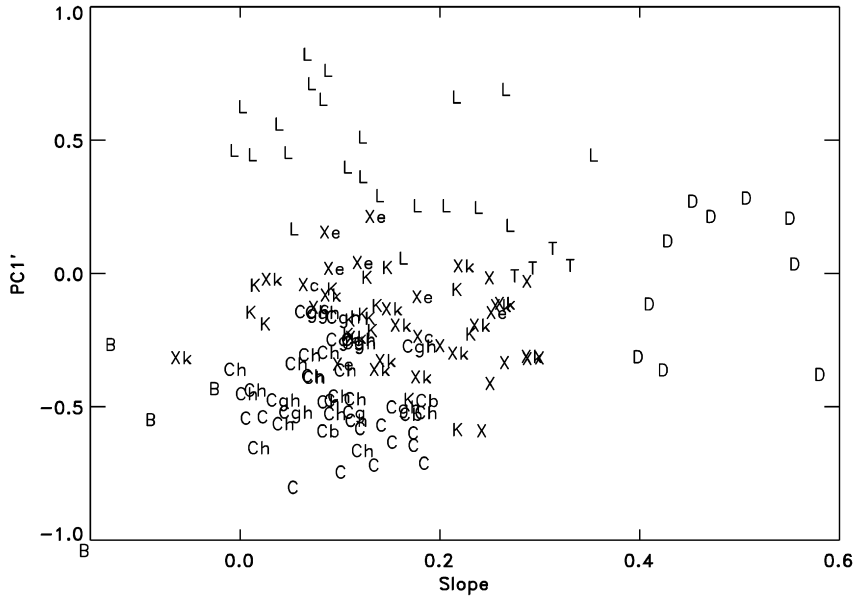

Fig. 10. The distribution of objects left of line α in slope versus PC1′ space. Here we see a clear separation for D- and T-types because of their high slopes. L-types are distinguished here by their positive PC1′ values. C-complex objects have the lowest PC′ values while X-complex and K-types reside between the L-types and C-complex.

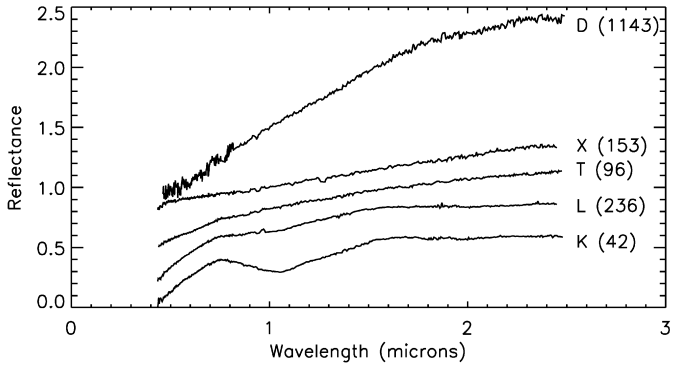

Fig. 11. Prototype examples of D-, L-, K-, T-, and X-class spectra.

absorption band centered near 0.7 μm. The Ch objects are well distinguished in PC1′ and PC4′ space, but a check must be done to distinguish them from the Cgh-type. The Cgh-class is similar to the Ch showing a 0.7-μm feature, but also has a more pronounced UV dropoff like the Cg-type. The C- and Cb-types separate in PC1′, PC4′, and PC5′. Figs. 12 and 13 show the C-complex plotted in PCA space. C-types are linear with neutral visible slopes and often have a slight rough bump around 0.6 μm and low but positive slope after 1.3 μm. Cb-types are linear with a small positive slope that begins around 1.1 μm. Cb objects were intermediate objects between the B- and C-classes in the Bus system (Bus and Binzel, 2002b). We keep the same notation, however, the near-infrared data shows, that Cb objects have low to moderate near-infrared slopes, while the visible slopes are low or negative. There is only one object (175 Andromache) in the Cg-class carrying over from the Bus (Bus, 1999; Bus and Binzel, 2002b) taxonomy. The Cg-class is character-

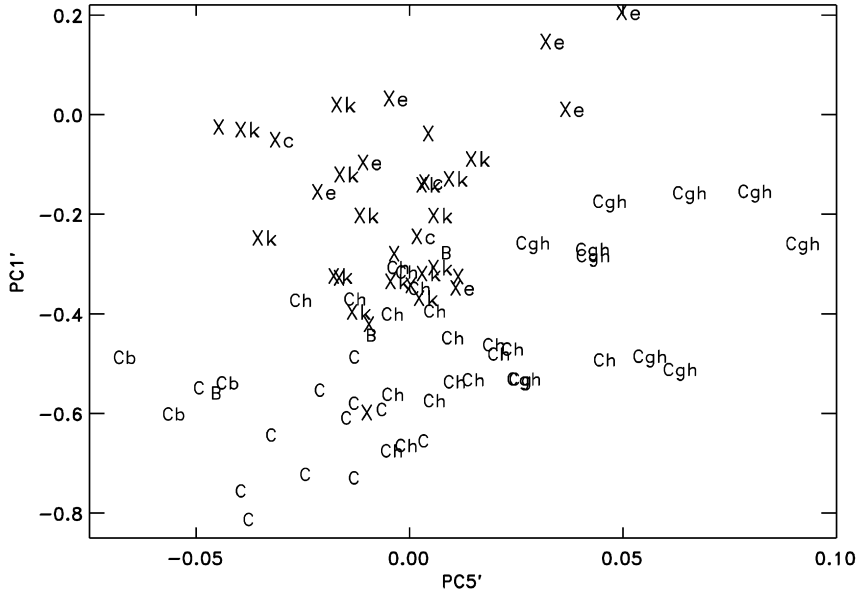

Fig. 12. Close examination of principal component distribution for the C-complex in PC5′ versus PC1′ space. This figure shows that C-types objects plot to the bottom left, while Xc-, Xe-, and Xk-types plot above the C-class with higher PC1′ values. Cgh-types have higher PC5′ values than other objects, and are plotted further right.

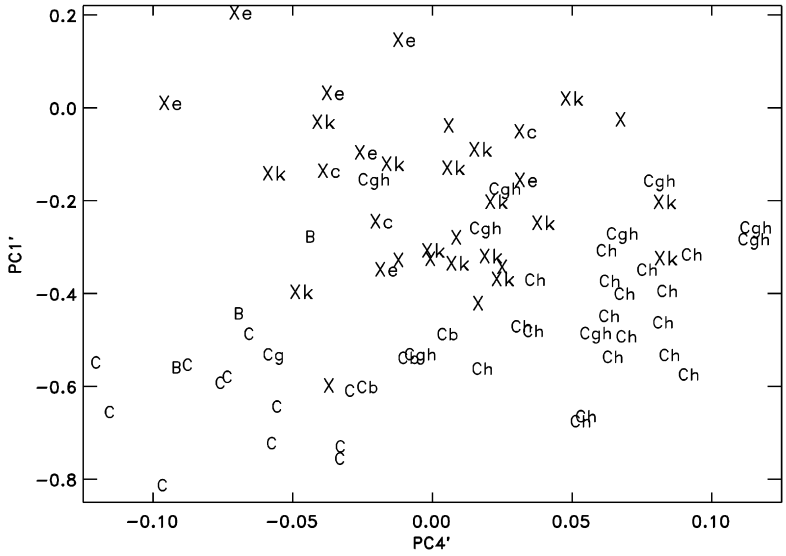

Fig. 13. view of the C-complex in PC4′ versus PC1′ space. Here we see the C-types plotting in the bottom left of the figure and the Ch-types and Cgh-types having higher PC4′ values plot further to the right.

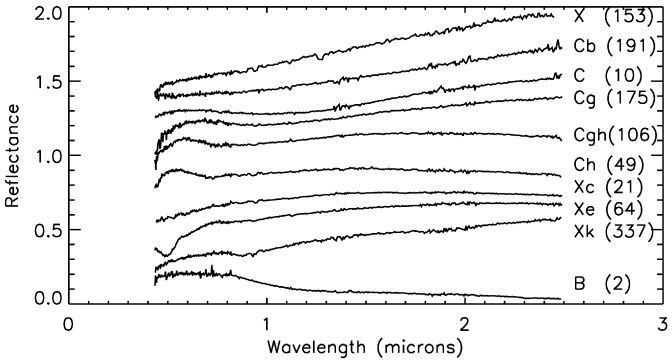

Fig. 14. Prototype examples for C- and X-complex spectra.

ized by a pronounced UV dropoff similar to the Cgh, but does not show the 0.7-μm feature that define Ch and Cgh. The classes Cg, Cgh, Ch, Xk, Xc, and Xe do not all separate cleanly in component space because their distinguishing features are weak and not well detected by the first five principal components. These classes often must be distinguished by visually detecting features described by Bus (1999). A summary of these features are described at the end of the flowchart, Appendix B. Fig. 14 shows typical spectra for classes within the C- and X-complexes.

4.6. A near-infrared-only classification method

For many objects, data exist in either the visible or near-infrared wavelength ranges but not both. While taxonomies such as the Bus system (Bus, 1999; Bus and Binzel, 2002b) are available for visible data, no system has been widely accepted for assigning classes to data existing only in the near-infrared. We have adapted our present taxonomy to interpret spectral data available only in the near-infrared range. This adaptive taxonomy is not meant to determine a definite class, but instead is an intermediate tool to indicate classes. We especially note that several classes in Section 4.5 are carried over unchanged from the Bus taxonomy and are based exclusively on features present at visible wavelengths. Assignment to these classes (Cg, Cgh, Xc, Xe, Xk) requires visible wavelength data, therefore objects in these classes cannot be recognized by near-infrared-only data.

To study the ability to classify objects having only near-infrared spectral data we took the same 371 objects used in the original taxonomy but included only data longward of 0.85 μm, again splining the data to smooth out noise. Our spline increments remained 0.05 μm covering the range of 0.85 to 2.45 μm resulting in 33 datapoints. We chose to normalize to unity at 1.2 μm, the closest splinefit wavelength value to 1.215 μm which is the isophotal wavelength for the J band based on the UKIRT filter set (Cohen et al., 1992). Next, we removed the slope from the data. As in the case with visible and near-infrared data we calculated the slope function without constraints, and then translate it in the y-direction to a value of unity at 1.2 μm. We then divide each spectrum by the slope function to remove the slope from the data set.

In Appendix C we provide a flowchart to define parameters within PCA_{ir} space using slope and the first five principal components from PCA_{ir} (see supplementary material for a table of IR eigenvectors and channel means). These principal components are denoted PCir1′ (to signify it is the first near-infrared principal component after slope has been removed), PCir2′, PCir3′, PCir4′, and PCir5′. Principal components greater than PCir5′ did not seem to contribute significant information distinguishing classes and were disregarded. In this case, we again start by separating end members and other classes with the most extreme PC_{ir} values in step 1. These classes include: A, Sa, V, Sv, O, R, D. Unfortunately the L-type objects may be mixed in with our definition of Sv- and R-types because they do not fully separate in all cases. In step 2 we address the S-complex, separating it into three groups. Because the entire 1-μm absorption band is not sampled some depth versus slope information is lost, making it difficult to distinguish between a steeply sloped spectrum with a shallow 1-μm feature and a spectrum with a lower slope but a deep 1-μm feature. Step three outlines the C- and X-complexes. The majority of C- and X-complex objects are defined by visible wavelength features, so as noted above, their relative classes are completely indistinguishable in an infrared-only spectrum. This is apparent in near-infrared principal component space; most C- and X-complex objects occupy the same region of space in all components. IR-only data therefore do not yield a unique outcome in Principal Component Analysis (PCA) and the data cannot formally be classified, however the possible types within each principal component space are ranked in order of their prevalence within the data set defining this taxonomy. In such cases where a unique class cannot be determined, visual inspection or quantitative comparison of residuals between

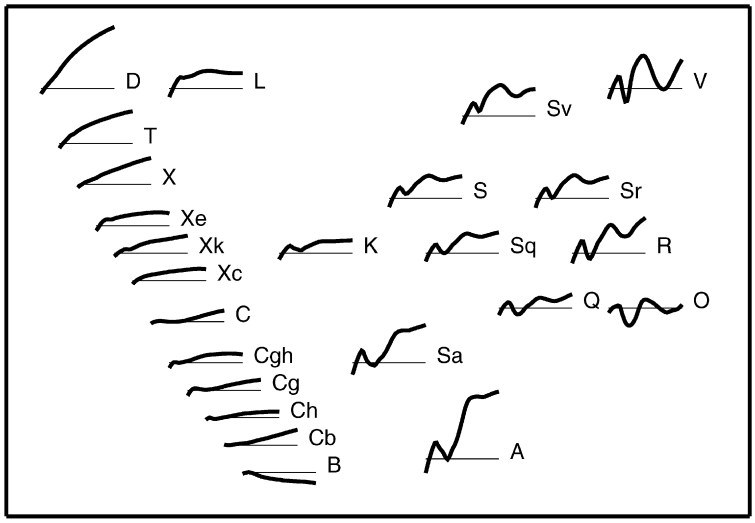

Fig. 15. A "key" showing all 24 taxonomic classes defined over 0.45–2.45 μm. The average spectra are plotted with constant horizontal and vertical scaling and are arranged in a way that approximates the relative position of each class in the primary spectral component space defined by slope, PC1′, and PC2′ (roughly following Fig. 2). Thus the depth and width of the 2-μm band generally increases lower left to upper right, and the depth and width of the 1-μm band increase moving downward and toward the right. For subtly featured objects slope increases from bottom to top. Due to the spectral complexity of the C- and X-complexes, the locations of some of these classes do not strictly follow the pattern. The horizontal lines to which each spectrum is referenced has a reflectance value of unity. This figure and description follows the style of Bus and Binzel (2002b, Fig. 15).

the input spectrum and the mean spectrum for each class may help reach a subjective conclusion for one or two classes that appear most likely.

5. Summary of the taxonomy

A "key" displaying the average spectrum for each of the 24 class in this taxonomy corresponding to their locations in principal component space is shown in Fig. 15. The subtly featured C- and X-complexes are to the left while classes displaying distinct 1- and 2-μm features are on the right, with the L-, K-, A-, and Sa-classes near the center. This figure is useful for comparing classes and recognizing the overall connection between them. Table 2 shows the evolution of the classes from the Bus (Bus, 1999; Bus and Binzel, 2002b) taxonomy to this work by noting classes that have changed and classes that also have the additional "w" notation.

We put this taxonomy in the context of past taxonomies by showing the range of Bus (Bus, 1999; Bus and Binzel, 2002b) and Tholen (1984) classes for objects contained within each class in this taxonomy in Table 3. It is clear that this visible plus near-infrared wavelength taxonomy is consistent with the spectral groupings of these two visible wavelength range classification systems, although there are some class changes for objects because of detail revealed only in the near-infrared wavelengths. In Table 4 we list the classes of featured objects in our system that fall under each of the Gaffey mineralogic classes (Gaffey et al., 1993). Taxonomy PCA is sensitive to spectral features which often, but not always, have mineralogic implications. Thus a direct mapping from PCA space to mineralogy can only be considered as a general trend. For example, in Fig. 2, the trend from A-type (interpreted as olivine-rich) to V-type (pyroxene-rich) goes from lower left to upper right. Examining the placement of Gaffey class S(I) (olivine-rich) through S(VII) (pyroxene-rich) follows this same trend. These objects generally fall in our S- and Sq-classes. A figure of the Gaffey labels plotted in our principal component space is available in the supplementary material.

A verbal description of each class is given in Table 5, explaining the key spectral features and attributes of each particular class and listing at most three objects within our sample that are considered prototypical of that class. This table also summarizes why

Table 2
Evolution from the Bus (1999) taxonomy to this work.[a]

Bus		New
A	⟹	A
B	⟹	B
C	⟹	C
Cb	⟹	Cb
Cg	⟹	Cg
Cgh	⟹	Cgh
Ch	⟹	Ch
D	⟹	D
Ld	↗ ↘	
L	⟹	L
K	⟹	K
O	⟹	O
Q	⟶	Q
R	⟹	R
Sq	⟶	Sr, Srw
	⟶	Sq, Sqw
Sr	⟶	Sa
Sa		
Sl	↘	S, Sw
Sk	↗	
S		
	⟶	Sv, Svw
T	⟹	T
V	⟶	V, Vw
X	⟹	X
Xc	⟹	Xc
Xe	⟹	Xe
Xk	⟹	Xk
Total: 26		24
Eliminated: Ld, Sk, Sl		Created: Sv

[a] w notation does not denote a distinct class. The double arrow is used for unchanged classes. The single arrow is used for classes that are modified.

the three Bus classes (Ld, Sl, Sk) were not continued in this taxonomy. A more quantitative summary of the taxonomy is given in the supplementary material where tables are provided with the mean value and standard deviation for the slope and the five principal component for each class, as well as the mean values and standard deviation for each wavelength channel for each class. The supplementary material also provides principal component scores for all

Table 3
Comparison with Bus and Tholen taxonomies.

Class	Classified this work	Classified by Bus	Classified by Tholen	Distribution by Bus class	Distribution by Tholen class
A	6	6	6	A(5) Sl(1)	A(5) S(1)
B	4	3	3	B(2) C(1)	B(1) F(1) BCF(1)
C	13	13	12	C(9) B(2) Cb(1) X(1)	C(6) CF(1) CU(1) CX(1) G(1) FC(1) M(1)
Cb	3	3	3	Cb(3)	CF(1) M(1) XC:(1)
Cg	1	1	1	Cg(1)	C(1)
Cgh	10	10	7	Cgh(5) Cg(1) Ch(2) C(1) Xc(1)	C(4) CU(1) G(1) E(1)
Ch	18	18	18	Ch(18)	C(10) G(4) CG(2) S(1) X(1)
D	16	12	7	D(4) X(3) T(3) Ld(1) L(1)	D(4) DU(1) ST(1) X(1)
K	16	15	12	K(10) S(1) L(1) Xk(1) Xc(1) Sq(1)	S(10) SU(1) T(1)
L	22	21	10	L(10) K(5) Ld(4) A(1) S(1)	S(7) STGD (1) TSD(1) I(1)
O	1	1	0	O(1)	
Q	8	5	2	Q(3) O(1) Sq(1)	Q(1) QU(1)
R	1	1	1	R(1)	R(1)
S	144	122	65	S(88) Sl(10) Sa(8) Sq(7) A(4) Sk(2) Sr(r) L(1)	S(60) AS(1) DU(1) QSV(1) SR(1) SU(1)
Sa	2	2	0	Sr(2)	
Sq	29	24	10	Sq(6) Sk(5) S(9) Sa(3) Sr(1)	S(9) SQ(1)
Sr	22	19	2	Sq(8) S(8) Sa(1) Sr(1)V(1)	S(2)
Sv	2	0	0		
T	4	4	4	T(4)	T(2) D(1) PCD(1)
V	17	11	3	V(9) R(2)	V(3)
X	4	3	3	X(3)	P(2) M(1)
Xc	3	3	3	X(2) Xk(1)	M(2) X(1)
Xe	7	7	6	Xe(7)	E(3) M(2) MU(1)
Xk	18	17	15	X(8) Xk(5) Xc(2) K(1) C(1)	M(5) P(3) X(2) S(1) T(1) C(1) CX(2)
Total	371	321	193		

Table 4
Comparison with Gaffey mineralogic classes.

Gaffey class	Num classified this work	Distribution by this work
S(I)	2	A(1) K(1)
S(II)	2	S(1) Sq(1)
S(II–III)	1	S(1)
S(III)	3	K(1) S(1) Sq(1)
S(III–IV)	1	S(1)
S(IV)	8	S(6) Sq(2)
S(V)	7	S(7)
S(VI)	2	S(2)
S(VI–VII)	1	S(1)
S(VII)	2	S(2)

371 objects used to create this taxonomy. Appendix B shows the flowchart to apply this taxonomy to new data. As in Bus (1999) it is a binary response decision tree used to locate the position of the object in multidimensional principal component space, which corresponds to the presence or absence of features that characterize each class.

6. Conclusion

An extended taxonomy was created using Principal Component Analysis and visible features to characterize visible and near-infrared wavelength spectra. The system, based on the Bus visible taxonomy from Bus (1999), and Bus and Binzel (2002b), has 24 classes compared to 26 in the Bus system. The changes in classes are summarized in Table 2. We eliminated three classes: Ld, Sl, and Sk. All the Bus S subclasses (Sa, Sl, Sk, Sq, Sr) had objects that merged back into the S-class, although many Sq objects remained Sq and two Sr objects were relabeled Sa. A new intermediate class, the Sv-class, was created as a link between the S- and V-classes. High-sloped S, Sq, Sr, Sv, V and Q objects were given a "w" notation to indicate possible weathering. Many of the classes that lie left of line α in PC2′ versus PC1′ space are either featureless or exhibit only small features at visible wavelengths identified by Bus (1999), and by Bus and Binzel (2002b). It is still necessary to use these visible features to distinguish the classes because there are no other corresponding features at near-infrared wavelengths. We have also devised a method to categorize data when solely the near-infrared wavelength range is available, however, without visible wavelength information, the near-infrared taxonomy supplement cannot definitively classify many types especially those in the C- and X-complex, as many of those classes are defined only by visible wavelength features. 371 objects were given types based on this new taxonomic system which was created using 6 dimensions including Slope and PC1′ through PC5′ of Principal Component Analysis. Within our sample, several classes remain relatively rare: only 6 objects fall into the A-class; 349 Dembowska and 3628 Boznemcova reside as the only objects in their respective R- and O-classes. Eight Q-class objects are all near-Earth asteroids. We note 1904 Massevitch as an outer main-belt V-type while 15 other V-type objects have inner main-belt orbits consistent with an association with Vesta.

Acknowledgments

We are grateful to numerous colleagues and students who have participated in or contributed to the collection or processing of data throughout the course of this project. These people include, but are not limited to, Mirel Birlan, Thomas Burbine, Jim Elliot, Susan Kern, Alison Klesman, Andrew Rivkin, Paul Schechter, Shaye Storm, Cristina Thomas, and Pierre Vernazza. Particular thanks for their advice and insight to Cristina Thomas, Pierre Vernazza, Jessica Sunshine, and Benoit Carry and to Nick Moscovitz for sharing principal component information of his data. We especially thank Maureen Bell and Beth Clark for sharing their unpublished spectra to improve class boundaries. Thanks to the anonymous referees for their many constructive improvements. Observations reported here were obtained at the Infrared Telescope Facility, which is operated by the University of Hawaii under Cooperative Agreement NCC 5-538 with the National Aeronautics and Space Administration, Science Mission Directorate, Planetary Astronomy Program. This paper

Table 5
Spectral class descriptions.

Class	Description	Prototypes
A	Deep and extremely broad absorption band with a minimum near 1 μm, may or may not have shallow 2-μm absorption band; very highly sloped.	246, 289, 863
B	Linear, negatively sloping often with a slight round bump around 0.6 μm and/or a slightly concave up curvature in the 1- to 2-μm region.	2, 3200
C	Linear, neutral visible slope often a slight rough bump around 0.6 μm and low but positive slope after 1.3. May exhibit slight feature longward of 1 μm.	1, 10, 52
Cb	Linear with a small positive slope that begins around 1.1 μm.	191, 210, 785
Cg	Small positive slope that begins around 1.3 μm and pronounced UV dropoff	175
Cgh	Small positive slope that begins around 1 μm and pronounced UV dropoff similar to Cg also includes a broad, shallow absorption band centered near 0.7 μm similar to Ch.	106, 706, 776
Ch	Small positive slope that begins around 1.1 μm and slightly pronounced UV dropoff also includes a broad, shallow absorption band centered near 0.7 μm.	19, 48, 49
D	Linear with very steep slope, some show slight curvature or gentle kink around 1.5 μm.	1143, 1542, 3248
K	Wide absorption band centered just longward of 1 μm, the left maximum and the minimum are sharply pointed and the walls of the absorption are linear with very little curvature.	42, 579, 742
L	Steep slope in visible region leveling out abruptly around 0.7 μm. There is often a gentle concave down curvature in the infrared with a maximum around 1.5 μm. There may or may not be a 2-μm absorption feature.	236, 402, 606
O	Very rounded and deep, "bowl" shape absorption feature at 1 μm as well as a significant absorption feature at 2 μm.	3628
Q	Distinct 1-μm absorption feature with evidence of another feature near 1.3 μm; a 2-μm feature exists with varying depths between objects.	1862, 3753, 5660
R	Deep 1- and 2-μm features; the 1-μm feature is much narrower than a Q-type, but slightly broader than a V-type.	349
S	Moderate 1- and 2-μm features. The 2-μm feature may vary in depth between objects.	5, 14, 20
Sa	Has a deep and extremely broad absorption band at 1 μm; has similar features to A-types but is less red.	984, 5261
Sq	Has a wide 1-μm absorption band with evidence of a feature near 1.3 μm like the Q-type, except the 1-μm feature is more shallow for the Sq.	3, 11, 43
Sr	Has a fairly narrow 1-μm feature similar to but more shallow than an R-type as well as a 2-μm feature.	237, 808, 1228
Sv	Has a very narrow 1-μm absorption band similar to but more shallow than a V-type as well as a 2-μm feature.	2965, 4451
T	Linear with moderate to high slope and often gently concaving down.	96, 308, 773
V	Very strong and very narrow 1-μm absorption and as well as a strong 2-μm absorption feature.	4, 1929, 2851
X	Linear with medium to high slope.	22, 87, 153
Xc	Low to medium slope and slightly curved and concave downward.	21, 97, 739
Xe	Low to medium slope similar to either Xc- or Xk-type, but with an absorption band feature shortward of 0.55 μm.	64, 77, 3103
Xk	Slightly curved and concave downward similar to Xc-type but with a faint to feature between 0.8 to 1 μm.	56, 110, 337
Ld	Diverged to L- and D-classes.	279 (D), 3734 (L)
Sk	Diverged to the S- and Sq-classes.	6585 (S), 3 (Sq)
Sl	Merged with the S-class.	17 (S), 30 (S)

includes data gathered with the 6.5 meter Magellan Telescopes located at Las Campanas Observatory, Chile. Observations in this paper were also obtained at the Kitt Peak National Observatory, National Optical Astronomy Observatory, which is operated by the Association of Universities for Research in Astronomy, Inc. (AURA) under cooperative agreement with the National Science Foundation. F.E.D. acknowledges funding from the Fulbright Program. This material is based upon work supported by the National Science Foundation under Grant 0506716 and NASA under Grant NAG5-12355. Any opinions, findings, and conclusions or recommendations expressed in this material are those of the authors and do not necessarily reflect the views of the National Science Foundation or NASA. Je présente mes excuses sincères pour ne pas avoir réussi à classifier l'asteroïde B612.

Supplementary material

The online version of this article contains additional supplementary material.

Please visit DOI: 10.1016/j.icarus.2009.02.005.

Appendix A

Table A
Observations[a] and designations.

Obj	Name	Tholen	Bus	This work	Date
1	Ceres	G	C	C	19-May-05
2	Pallas	B	B	B	29-Mar-01
3	Juno	S	Sk	Sq	17-Mar-03
4	Vesta	V	V	V	09-Oct-00
5	Astraea	S	S	S	20-Feb-04
7	Iris	S	S	S	20-Feb-04
8	Flora	S		Sw	16-Sep-02[b]
10	Hygiea	C	C	C	19-Feb-04
11	Parthenope	S	Sk	Sq	13-Nov-05
13	Egeria	G	Ch	Ch	19-May-05
14	Irene	S	S	S	17-May-01
15	Eunomia	S	S	K	19-Feb-04
16	Psyche	M	X	Xk	09-Oct-00
17	Thetis	S	Sl	S	15-Aug-01
18	Melpomene	S	S	S	22-Jun-01
19	Fortuna	G	Ch	Ch	29-Jan-06
20	Massalia	S	S	S	22-Jun-01
21	Lutetia	M	Xk	Xc	22-Sep-04
22	Kalliope	M	X	X	25-Oct-06
24	Themis	C	B	C	08-Oct-05

(*continued on next page*)

Table A (*continued*)

Obj	Name	Tholen	Bus	This work	Date
25	Phocaea	S	S	S	30-Jan-01
26	Proserpina	S	S	S	24-Aug-01
27	Euterpe	S	S	S	22-Sep-04
28	Bellona	S	S	S	13-Jan-02
29	Amphitrite	S	S	S	29-Jan-01
30	Urania	S	Sl	S	08-Oct-00
32	Pomona	S	S	Sw	30-Jan-01
33	Polyhymnia	S	Sq	S	06-Mar-02
34	Circe	C	Ch	Ch	20-Feb-04
37	Fides	S	S	S	15-Aug-01
38	Leda	C	Cgh	Cgh	05-Jul-03
39	Laetitia	S	S	Sqw	14-Aug-01
40	Harmonia	S	S	S	16-Oct-04
41	Daphne	C	Ch	Ch	10-May-08
42	Isis	S	L	K	21-Jun-01
43	Ariadne	S	Sk	Sq	22-Nov-05
48	Doris	CG	Ch	Ch	08-Oct-05
49	Pales	CG	Ch	Ch	02-Aug-03
50	Virginia	X	Ch	Ch	05-Jul-03
51	Nemausa	CU	Ch	Cgh	15-Jun-04
52	Europa	CF	C	C	28-Jun-06
54	Alexandra	C	C	Cgh	27-Oct-02
55	Pandora	M	X	Xk	29-Jan-06
56	Melete	P	Xk	Xk	22-Sep-04
57	Mnemosyne	S	S	S	01-Jun-02
58	Concordia	C	Ch	Ch	02-Aug-03
61	Danae	S	S	S	08-Oct-00
63	Ausonia	S	Sa	Sw	30-Sep-03
64	Angelina	E	Xe	Xe	30-Jan-01
65	Cybele	P	Xc	Xk	30-Sep-03
66	Maja	C	Ch	Ch	22-Nov-05
67	Asia	S	S	S	16-Jun-04
69	Hesperia	M	X	Xk	11-May-05
70	Panopaea	C	Ch	Cgh	29-Sep-02
73	Klytia	S		S	16-Oct-03[b,c]
76	Freia	P	X	C	05-Sep-05
77	Frigga	MU	Xe	Xe	25-Oct-06
78	Diana	C	Ch	Ch	31-Oct-05
82	Alkmene	S	Sq	S	24-Aug-01
84	Klio	G	Ch	Ch	02-Aug-03
85	Io	FC	B	C	02-Aug-03
87	Sylvia	P	X	X	04-Sep-05
90	Antiope	C	C	C	05-Sep-05
92	Undina	X	Xc	Xk	08-Oct-00
93	Minerva	CU	C	C	27-Apr-03
96	Aegle	T	T	T	28-Jan-06
97	Klotho	M	X	Xc	08-Oct-05
99	Dike	C	Xk	Xk	13-Nov-05
101	Helena	S	S	S	22-Dec-06
103	Hera	S	S	S	14-Aug-01
105	Artemis	C	Ch	Ch	02-Aug-03
106	Dione	G	Cgh	Cgh	02-Aug-03
108	Hecuba	S	Sl	Sw	06-Mar-02
110	Lydia	M	X	Xk	29-Jan-01
111	Ate	C	Ch	Ch	22-Sep-04
114	Kassandra	T	Xk	K	28-Jun-06
115	Thyra	S	S	S	06-Mar-02
119	Althaea	S	Sl	S	21-Jun-01
128	Nemesis	C	C	C	02-Aug-03
130	Elektra	G	Ch	Ch	29-Mar-01
131	Vala	SU	Xc	K	20-Jul-06
132	Aethra	M	Xe	Xe	05-Sep-05
133	Cyrene	SR	S	S	22-Jun-01
147	Protogeneia	C	C	C	02-Aug-03
150	Nuwa	CX	Cb	C	02-Aug-03
151	Abundantia	S	Sl	Sw	13-Nov-05
153	Hilda	P	X	X	10-May-05
158	Koronis	S	S	S	16-Mar-03
160	Una	CX	C	Xk	5-Jul-03
170	Maria	S	S	S	22-Jun-01
175	Andromache	C	Cg	Cg	13-Nov-05
180	Garumna	S	Sq	Sr	28-Sep-02
181	Eucharis	S	Xk	Xk	30-Sep-03

Table A (*continued*)

Obj	Name	Tholen	Bus	This work	Date
188	Menippe	S	S	S	15-Apr-02
191	Kolga	XC:	Cb	Cb	12-Apr-05
192	Nausikaa	S	Sl	Sw	30-Apr-06
199	Byblis		X	D	17-Mar-03
201	Penelope	M	X	Xk	19-Feb-04
205	Martha	C	Ch	Ch	02-Aug-03
210	Isabella	CF	Cb	Cb	13-Nov-05
214	Aschera	E	Xc	Cgh	24-Oct-04
216	Kleopatra	M	Xe	Xe	17-Jun-02
221	Eos	S	K	K	08-Oct-00
226	Weringia		S	S	06-Mar-02
233	Asterope	T	K	Xk	29-Sep-02
234	Barbara	S	Ld	L	22-Dec-06
236	Honoria	S	L	L	01-May-06
237	Coelestina	S	S	Sr	15-Apr-02
243	Ida	S	S	Sw	17-Mar-03
244	Sita		Sa	Sw	29-Mar-01
246	Asporina	A	A	A	09-Mar-05
250	Bettina	M	Xk	Xk	16-Oct-03
258	Tyche	S	S	S	24-Aug-01
264	Libussa	S	S	S	19-May-05
266	Aline	C	Ch	Ch	05-Sep-05
267	Tirza	DU	D	D	02-Aug-03
269	Justitia		Ld	D	11-May-05
278	Paulina		S	S	31-May-02
279	Thule	D	X	D	08-Jan-05
288	Glauke	S	S	S	29-Sep-02
289	Nenetta	A	A	A	04-Sep-00
295	Theresia	S	S	Sw	28-Sep-02
308	Polyxo	T	T	T	18-Apr-05
322	Phaeo	X	X	D	29-Sep-02
337	Devosa	X	X	Xk	28-Sep-02
345	Tercidina	C	Ch	Ch	08-Oct-05
346	Hermentaria	S	S	S	31-May-02
349	Dembowska	R	R	R	22-Jun-01
352	Gisela	S	Sl	Sw	22-Jun-01
354	Eleonora	S	Sl	A	15-Apr-02
359	Georgia	CX	X	Xk	30-Jan-01
371	Bohemia	QSV	S	S	14-Aug-01
378	Holmia	S	S	S	14-Apr-02
387	Aquitania	S	L	L	27-Apr-03
389	Industria	S	S	S	24-Aug-01
402	Chloe	S	K	L	19-Feb-01
403	Cyane	S	S	S	27-Apr-03
433	Eros	S	S	Sw	17-Aug-02
434	Hungaria	E	Xe	Xe	23-Aug-01
444	Gyptis	C	C	C	15-Aug-01
446	Aeternitas	A	A	A	14-Aug-01
453	Tea	S	S	Sw	15-Aug-01
456	Abnoba		S	S	17-Jun-02
460	Scania		K	L	17-Jun-02
485	Genua		S	S	06-Mar-02
512	Taurinensis	S	S	Sqw	16-Oct-04
513	Centesima	S	K	K	29-Mar-01
532	Herculina	S	S	S	21-Jun-01
570	Kythera	ST	T	D	20-Feb-04
579	Sidonia	S	K	K	20-Feb-01
596	Scheila	PCD	T	T	01-Jun-02
599	Luisa	S	K	L	19-Feb-01
606	Brangane	TSD	K	L	29-Sep-02
625	Xenia		Sa	Sw	20-Feb-01
631	Philippina	S	S	S	29-Sep-02
653	Berenike	S	K	K	17-Mar-03
661	Cloelia	S	K	K	16-Mar-03
670	Ottegebe		S	S	29-Sep-02
673	Edda	S	S	L	21-Jun-01
675	Ludmilla	S	S	Sw	15-Apr-02
679	Pax	I	K	L	19-Feb-01
688	Melanie		C	C	28-Sep-02
699	Hela	S	Sq	S	08-Jan-05
706	Hirundo		Cgh	Cgh	30-Jan-06
716	Berkeley	S	S	S	24-Aug-01
719	Albert			S	23-Aug-01[d]

Table A (*continued*)

Obj	Name	Tholen	Bus	This work	Date
720	Bohlinia	S	Sq	Sq	09-Oct-00
729	Watsonia	STGD	L	L	14-Aug-01
739	Mandeville	X	X	Xc	28-Sep-02
742	Edisona	S	K	K	16-Mar-03
773	Irmintraud	D	T	T	22-Sep-04
776	Berbericia	C	Cgh	Cgh	12-Apr-05
782	Montefiore	S	Sl	Sw	22-Jun-01
785	Zwetana	M	Cb	Cb	19-May-05
789	Lena		X	Xk	17-Aug-02
793	Arizona	DU:	S	S	28-Sep-02
808	Merxia		Sq	Sr	14-Aug-01
824	Anastasia	S	L	L	14-Aug-01
832	Karin			S	05-Jul-03[e]
847	Agnia	S	S	S	19-Feb-01
863	Benkoela	A	A	A	14-Jan-02
908	Buda		L	D	20-Jul-06
913	Otila		Sa	Sw	15-Aug-01
925	Alphonsina	S	S	S	28-Sep-02
929	Algunde		S	S	21-Jun-01
944	Hidalgo	D		D	22-Sep-04[e]
984	Gretia		Sr	Sa	29-Sep-02
985	Rosina		S	S	11-May-05
1011	Laodamia	S	Sr	Sw	12-Jan-02
1020	Arcadia		S	Sr	17-Mar-03
1036	Ganymed	S	S	S	09-Mar-05
1065	Amundsenia		S	S	08-Mar-05
1094	Siberia		Xk	Xk	16-Mar-03
1126	Otero		A	Sw	20-Feb-01
1131	Porzia		S	S	11-May-05
1139	Atami	S	S	Sw	05-Sep-05
1143	Odysseus	D		D	10-Jun-05[b]
1147	Stavropolis		S	Sw	15-Aug-01
1148	Rarahu	S	K	K	29-Mar-01
1198	Atlantis			Sw	28-Oct-02[b]
1204	Renzia		S	Sw	10-Mar-05
1228	Scabiosa		S	Sr	16-Mar-03
1300	Marcelle		Cg	Cgh	25-Oct-06
1329	Eliane	S	S	Sqw	17-Aug-02
1332	Marconia		Ld	L	10-Jun-05
1350	Rosselia	S	Sa	S	21-Jun-01
1374	Isora		Sq	Sq	20-Feb-04
1433	Geramtina		S	S	17-Aug-02
1459	Magnya			Vw	20-Feb-01[b]
1471	Tornio		T	D	08-Oct-05
1494	Savo		Sa	Sqw	25-Oct-06
1508	Kemi	BCF	C	B	19-Feb-04
1542	Schalen		D	D	18-Apr-05
1565	Lemaitre		Sq	S	03-Mar-05
1620	Geographos	S	S	S	29-Jan-01
1640	Nemo		S	S	08-Mar-05
1642	Hill		S	S	15-Aug-01
1658	Innes	AS		Sw	30-Jan-01[c]
1659	Punkaharju		S	S	15-Mar-02
1660	Wood		S	S	08-Mar-05
1662	Hoffmann		Sr	Sr	17-Mar-03
1667	Pels		Sa	Sw	28-Oct-02
1685	Toro	S	S	Sq	08-May-02[h]
1751	Herget		S	S	22-Jun-01
1807	Slovakia		S	Sqw	15-Sep-04
1839	Ragazza		S	S	29-Mar-01
1848	Delvaux		S	S	15-Aug-01
1858	Lobachevskij		L	S	14-Apr-02
1862	Apollo	Q	Q	Q	13-Nov-05
1864	Daedalus	SQ	Sr	Sq	29-Mar-01
1866	Sisyphus		S	Sw	21-Nov-06
1903	Adzhimushkaj		K	K	17-Mar-03
1904	Massevitch		R	V	04-Sep-00
1916	Boreas	S		Sw	14-Aug-01[d]
1929	Kollaa		V	V	19-Feb-01
1943	Anteros	S		Sw	12-Jan-02[g,h]
1980	Tezcatlipoca	SU	Sl	Sw	25-Oct-06
2035	Stearns	E	Xe	Xe	28-Oct-02

Table A (*continued*)

Obj	Name	Tholen	Bus	This work	Date
2042	Sitarski		Sq	Sr	23-Aug-01
2045	Peking		V	V	14-Jan-02
2063	Bacchus		Sq	Sq	19-May-05
2064	Thomsen		S	Sqw	29-Jun-06
2074	Shoemaker			Sw	30-Sep-03[b]
2085	Henan		L	L	14-Apr-02
2099	Opik	S	Ch	Ch	08-Oct-05
2107	Ilmari		S	Sw	29-Jan-06
2157	Ashbrook		S	S	16-Mar-03
2246	Bowell	D	D	D	17-Apr-05
2335	James			S	30-Oct-05
2353	Alva		S	S	31-May-02
2354	Lavrov		L	L	17-Mar-03
2378	Pannekoek		Cgh	Cgh	11-May-05
2386	Nikonov		S	S	17-Jun-02
2396	Kochi		Sa	S	15-Aug-01
2401	Aehlita		S	S	17-Aug-02
2442	Corbett			V	15-Sep-02[c]
2448	Sholokhov		L	L	16-Mar-03
2501	Lohja	A	A	A	12-Jan-02
2504	Gaviola		Sq	Sr	27-Apr-03
2521	Heidi		S	S	13-Jan-02
2566	Kirghizia		V	V	16-Sep-02
2579	Spartacus		V	V	10-Oct-00
2715	Mielikki		A	Sw	15-Aug-01
2732	Witt		A	L	15-Aug-01
2851	Harbin		V	V	24-Aug-01
2873	Binzel		Sq	Sq	13-Jan-02
2875	Lagerkvist		S	S	16-Mar-02
2911	Miahelena		S	Sw	17-Mar-03
2912	Lapalma		V	V	20-Feb-01
2957	Tatsuo		K	K	16-Mar-03
2965	Surikov			Sv	10-May-05[b]
2977	Chivilikhin		S	S	28-Sep-02
3028	Zangguoxi		K	K	16-Sep-02
3102	Krok	S		Sqw	09-Oct-00[d]
3103	Eger		Xe	Xe	21-Jun-01[i]
3122	Florence		S	Sqw	26-Jan-04
3155	Lee		V	V	22-Jun-01
3198	Wallonia		S	Sqw	10-May-05
3199	Nefertiti	S	Sq	K	03-Mar-05
3200	Phaethon	F	B	B	10-Dec-04
3248	Farinella		D	D	18-Apr-05
3255	Tholen		S	S	16-Sep-02
3317	Paris		T	D	01-May-06
3363	Bowen		Sq	Sr	15-Apr-02
3395	Jitka		Sr	S	19-Feb-01
3402	Wisdom			S	30-Sep-03[e]
3430	Bradfield		Sq	S	17-Jun-02
3491	Fridolin		Sq	S	17-Jun-02
3511	Tsvetaeva		S	Srw	15-Apr-02
3628	Boznemcova		O	O	30-Apr-06
3635	Kreutz		S	Srw	12-Nov-05
3701	Purkyne		S	S	14-Aug-01
3734	Waland		Ld	L	24-Aug-01
3753	Cruithne		Q	Q	08-Oct-05
3788	Steyaert		S	S	17-Mar-03
3844	Lujiaxi		L	L	27-Apr-03
3858	Dorchester		Sa	Srw	20-Feb-04
3873	Roddy		S	Sw	28-Oct-02
3903	Kliment Ohridski		Sq	S	16-Sep-02
3908	Nyx	V		V	15-Sep-04
3910	Liszt		S	S	17-Aug-02
3920	Aubignan		Sa	Sqw	16-Sep-02
3949	Mach		Sq	Sq	24-Aug-01
4038	Kristina			Vw	28-Oct-02[d]
4055	Magellan	V		V	11-Apr-05[d]
4179	Toutatis		Sk	Sq	15-Sep-04
4188	Kitezh		V	V	14-Aug-01
4197	1982 TA		Sq	Sq	30-Sep-03
4352	Kyoto		S	S	17-Jun-02
4407	Taihaku		Sa	Sqw	24-Aug-01

(*continued on next page*)

Table A (*continued*)

Obj	Name	Tholen	Bus	This work	Date
4417	Lecar		S	Sw	24-Aug-01
4451	Grieve			Svw	14-Jan-02[d]
4558	Janesick		S	Sr	15-Jun-04
4570	Runcorn		Sa	Sw	21-Jun-01
4688	1980 WF	QU		Q	29-Jan-01[d]
4713	Steel		A	Sw	14-Apr-02
4737	Kiladze		L	L	17-Jun-02
4995	Griffin		S	S	28-Oct-02
5013	Suzhousanzhong		Sl	Sw	14-Jan-02
5111	Jacliff		R	V	05-Sep-05
5143	Heracles		O	Q	25-Oct-06
5230	Asahina		S	S	5-Sep-05
5261	Eureka		Sr	Sa	19-May-05
5379	Abehiroshi		V	Sr	3-Jun-06
5401	Minamioda		S	Sw	16-Mar-03
5407	1992 AX		Sk	S	13-Jan-02
5587	1990 SB		Sq	Sr	28-Mar-01
5604	1992 FE			V	29-Mar-01[f]
5641	McCleese		A	Sw	12-Apr-05
5660	1974 MA		Q	Q	22-Aug-93
5685	Sanenobufukui		S	S	29-Mar-01
5817	Robertfrazer		S	Sr	22-Sep-04
5840	Raybrown		Ld	L	24-Aug-01
6047	1991 TB1		S	S	8-Oct-05
6239	Minos			Sqw	26-Jan-04[e]
6386	Keithnoll		S	S	3-Mar-05
6411	Tamaga			B	20-Feb-04[e]
6455	1992 HE		S	Srw	28-Oct-02
6585	O'Keefe		Sk	S	25-Oct-06
7341	1991 VK		Sq	Q	16-Mar-02
7763	Crabeels		L	L	1-Jun-02
8334	1984 CF		S	S	17-Mar-03
8444	Popovich			S	30-Sep-03[e]
17274	2000 LC16			D	10-Oct-00[d]
18736	1998 NU			Sw	30-Jan-01[d]
19127	Olegefremov			Srw	30-Sep-03[e]
19356	1997 GH3		S	Sq	30-Jan-01
20786	2000 RG62			Sq:	1-Sep-03[d]
20790	2000 SE45			S	29-Jan-01[d]
22771	1999 CU3			S	16-Oct-03[d]
24475	2000 VN2			Sw	29-Mar-01[d]
25330	1999 KV4			Xk:	27-Oct-02[d]
35107	1991 VH		Sk	Sq	27-Dec-02
36284	2000 DM8			K	16-Mar-02[d]
53435	1999 VM40			Srw	25-Oct-06[g]
54690	2001 EB			S	28-Mar-01[d]
66146	1998 TU3			Q	1-Sep-03[e]
86450	2000 CK33			L	29-Jan-01[d]
86819	2000 GK137			Sq	9-Oct-00[d]
89355	2001 VS78			Sr	16-Mar-02
98943	2001 CC21			Sw	24-Oct-04[f]
99907	1989 VA		Sq	Sr	27-Oct-02
137062	1998 WM		Sq	Sr	27-Oct-02
138258	2000 GD2			Sq	16-Oct-03[d]
162058	1997 AE12			Q	15-Mar-02
162781	2000 XL44			S	29-Jan-01[d]
2000PG3				D	4-Sep-00[d]
2001TX16				X	15-Mar-02[d]
2001XN254				S	14-Apr-02[d]
2002AA				S	13-Jan-02[d]
2002AV				S	13-Jan-02[d]

[a] All visible data are from Bus (1999), Bus and Binzel (2002a) and Bus and Binzel (2002b) unless marked by a footnote.
[b] Visible data: Xu (1994); Xu et al. (1995).
[c] Visible data: Burbine (2000); Burbine and Binzel (2002).
[d] Binzel et al. (2004c).
[e] Visible data: This work. 832, 03-Mar-05; 944, 14-June-01; 3402, 01-Sep-03; 6239 29-Dec-03; 6411, 29-Dec-03; 8444, 28-Dec-03; 19127 28-Dec-03; 66146, 3-Sep-03. All these observations were taken on telescope KPNO 4 m except 944 on Magellan 6.5 m.
[f] Visible data: Binzel et al. (2004b).
[g] Visible data: Binzel et al. (2001).
[h] Near-IR data: Binzel et al. (2004a).
[i] Near-IR data: Rivkin et al. (2005).

Appendix B

Table B
Visible–IR flowchart.

Vis–IR step 1			
Does it satisfy all: $PC1' < -0.30$, $PC3' \geqslant 0.20$, Slope $\geqslant 0.40$	no →	Vis–IR step 2	
↓ yes			
Does it satisfy: $0.55 \leqslant$ Slope < 1.5	yes →	A	
↓ no			
Does it satisfy: $0.40 \leqslant$ Slope < 0.55	yes →	Sa	
↓ no			
Indeterminate			
Vis–IR step 2			
Does it lie below line α?	yes →	Vis–IR step 3	
↓ no			
Does it line on or above line δ?	yes →	V	and if Slope $\geqslant 0.25$ → Add w notation Vw
↓ no			
Does satisfy both: Lies on or below line η. Lies on or above θ and below δ	yes →	O	
↓ no			
Does satisfy both: Lies on or below line η. Lies on or above α and below θ.	yes →	Q	and if Slope $\geqslant 0.25$ → Add w notation Qw
↓ no			
Does satisfy both: Lies on above line η. Lies on or above γ and below δ	yes →	R	
↓ no			
Vis–IR S-complex			
Vis–IR step 3			
Does it satisfy both: $0.38 \leqslant$ Slope < 1.5, $-0.44 < PC1' < 0.4$	yes →	D	A: Prominent 1-μm feature.
↓ no			
Does it satisfy all: $0.25 <$ Slope < 0.38, $-0.28 < PC2' < -0.20$, $-0.20 < PC3' < -0.12$	yes →	T	
↓ no			
Does it satisfy both: $0.07 < PC1' < 1.00$, $-0.5 < PC2' < -0.15$	yes →	L, Xe	Xe: Shows feature at 0.49 μm.
↓ no			
Does it satisfy all: $-0.075 < PC3' < 0.14$, $-0.20 \leqslant PC2' < -0.10$, $-0.80 < PC1' < -0.10$	yes →	K, Xe	Xe: Shows feature at 0.49 μm.
↓ no			
Vis–IR C- and X-complexes			
Vis–IR S-complex			
Does it satisfy both: Lies below β and above ζ	yes →	S	and if Slope $\geqslant 0.25$ → Add w notation Sw
↓ no			
Does it satisfy all: Lies on or above α and below β, Lies above η and on or below ζ	yes →	Sq	and if Slope $\geqslant 0.25$ → Add w notation Sqw
↓ no			

Table B (*continued*)

Does it satisfy all: Lies on or above β and below γ Lies above η and on or below ε ↓no	yes →	Sr	and if Slope ⩾ 0.25 → Add w notation Srw
Does it satisfy all: Lies on or above β Lies above ε and below γ ↓no	yes →	Sv	and if Slope ⩾ 0.25 → Add w notation Svw
Indeterminate			
Vis–IR C- and X-complexes			
Does it satisfy all: -0.2 < Slope < 0 -1.2 < PC1′ < 0 PC4′ < 0 ↓no	yes →	B	
Does it satisfy: 0.2 < Slope < 0.38 ↓no	yes →	X, Xk, Xe, C	X: Featureless. Xk: Shows feature between 0.8–1 μm. Xe: Shows feature at 0.49 μm. C: Shows feature between 1–1.3 μm.
Does it satisfy all: 0.01 < PC4′ < 0.14 −0.75 < PC1′ < −0.27 Reflectance at 0.45 μm < 0.92. ↓no	yes →	Cgh, Xk	Cgh: Shows feature at 0.7 μm. Xk: Shows feature between 0.8–1 μm.
Does it satisfy both: 0.01 < PC4′ < 0.14 −0.75 < PC1′ < −0.27 ↓no	yes →	Ch, Xk	Ch: Shows feature at 0.7 μm. Xk: Shows feature between 0.8–1 μm.
Does it satisfy both: −0.04 < PC4′ < 0.02 −0.07 < PC5′ < −0.04 ↓no	yes →	Cb	
Does it satisfy both: −0.85 < PC1′ < −0.45 −0.06 < PC5′ < 0.02 ↓no	yes →	C, Ch, Xk	C: Shows feature between 1–1.3 μm. Ch: Shows feature at 0.7 μm. Xk: Shows feature between 0.8–1 μm.
Does it satisfy both: 0.02 ⩽ PC5′ < 0.1 −0.60 < PC1′ < −0.16 ↓no	yes →	Cgh, Cg, Xk	Cgh: Shows feature at 0.7 μm. Xk: Shows feature between 0.8–1 μm.
Does it satisfy both: −0.45 ⩽ PC1′ < 0.1 −0.06 < PC5′ < 0.05 ↓no	yes →	Xk, Xc, Xe, C, Ch	Xk: Shows feature between 0.8–1 μm. Xc: Featureless. Xe: Shows feature at 0.49 μm. C: Shows feature between 1–1.3 μm. Ch: Shows Shows feature at 0.7 μm.
Does it satisfy both: −0.1 ⩽ PC1′ < 0.3 −0.5 < PC2′ < −0.2 ↓no	yes →	Xe, L	Xe: Shows feature at 0.49 μm.
Indeterminate			

Vis–IR checks[a] for Cg, Cgh, Ch, Xc, Xe, Xk		Vis–IR equations	
Cg	Strong UV absorption feature before 0.55 μm	$PC1' = -3PC2' - 0.28$	Line α
Ch	Moderately shallow absorption feature around 0.7 μm	$PC1' = -3PC2' + 0.35$	Line β
Cgh	Strong UV absorption feature like Cg and 0.7-μm feature like Ch (Reflectance at 0.45 μm < 0.92)	$PC1' = -3PC2' + 1.00$ $PC1' = -3PC2' + 1.50$	Line γ Line δ
Xc	Red and featureless with slight concave down curvature	$PC1' = \frac{1}{3}PC2' + 0.50$	Line ε
Xe	Concave-up absorption feature before 0.55 μm	$PC1' = \frac{1}{3}PC2' - 0.10$	Line ζ
Xk	Red shortward of 0.75 μm and generally flat longward of 0.75 μm	$PC1' = \frac{1}{3}PC2' - 0.50$ $PC1' = -3PC2' + 0.70$	Line η Line θ

[a] These spectral features are originally defined in Bus (1999) and Table 2 of Bus and Binzel (2002b).

Appendix C

Table C
IR flowchart.

IR step 1: End members		
Does it satisfy: PCir1′ ⩽ 0.5 ↓no	no →	V
Does it satisfy all: 0.29 ⩽ PCir1′ < 0.5 PCir5′ ⩽ 0.05 ↓no	yes →	Sv, Sr
Does it satisfy all: PCir2′ ⩽ −0.5 PCir4′ ⩾ 0.15 −0.40 < PCir1′ ⩽ 0 ↓no	yes →	O
Does it satisfy all: 0.25 ⩽ PCir2′ < 0.5 PCir5′ ⩾ 0.06 PCir3′ ⩾ 0.05 ↓no	yes →	R
Does it satisfy all: Below line 1 PCir3′ ⩽ −0.02 $Slope_{ir}$ ⩾ 0.24 ↓no	yes →	D
Does it satisfy all: PCir1′ ⩽ −0.4 PCir2′ ⩽ −0.2 PCir4′ ⩾ −0.07 $Slope_{ir}$ ⩾ 0.5 PCir3′ ⩾ 0 ↓no	yes →	A
Does it satisfy all: PCir1′ ⩽ −0.4 ↓no	yes →	Sa
Step 2		
IR step 2: S-complex		
Does it lie on or above line 1 and 2? ↓no	yes →	S, Sr, Sq
Does it lie on or above line 1 and between line 2 and 3? ↓no	yes →	S, Sq, Q, L, K
Does it line on or above line 1 and on or between line 3 and 4? ↓no	yes →	K, L, Sq
IR step 3		
IR step 3: C- and X-complexes		
Does it satisfy: Below line 1 and on or between 3 and 4? ↓no	yes →	X-, C-complexes, L, K, T
Does it satisfy: Below line 1 and between 2 and 3? ↓no	yes →	X-, C-complexes
Does it satisfy: Below line 1 and 4? ↓no	yes →	C, B, L, Cb, X
Indeterminate		
IR equations		
$PCir3' = PCir2' - 0.08$		Line 1
$PCir1' = PCir2' + 0.15$		Line 2
$PCir1' = PCir2' - 0.10$		Line 3
$PCir1' = PCir2' - 0.40$		Line 4

Appendix D. Reflectance spectra for 371 asteroids defining this taxonomy

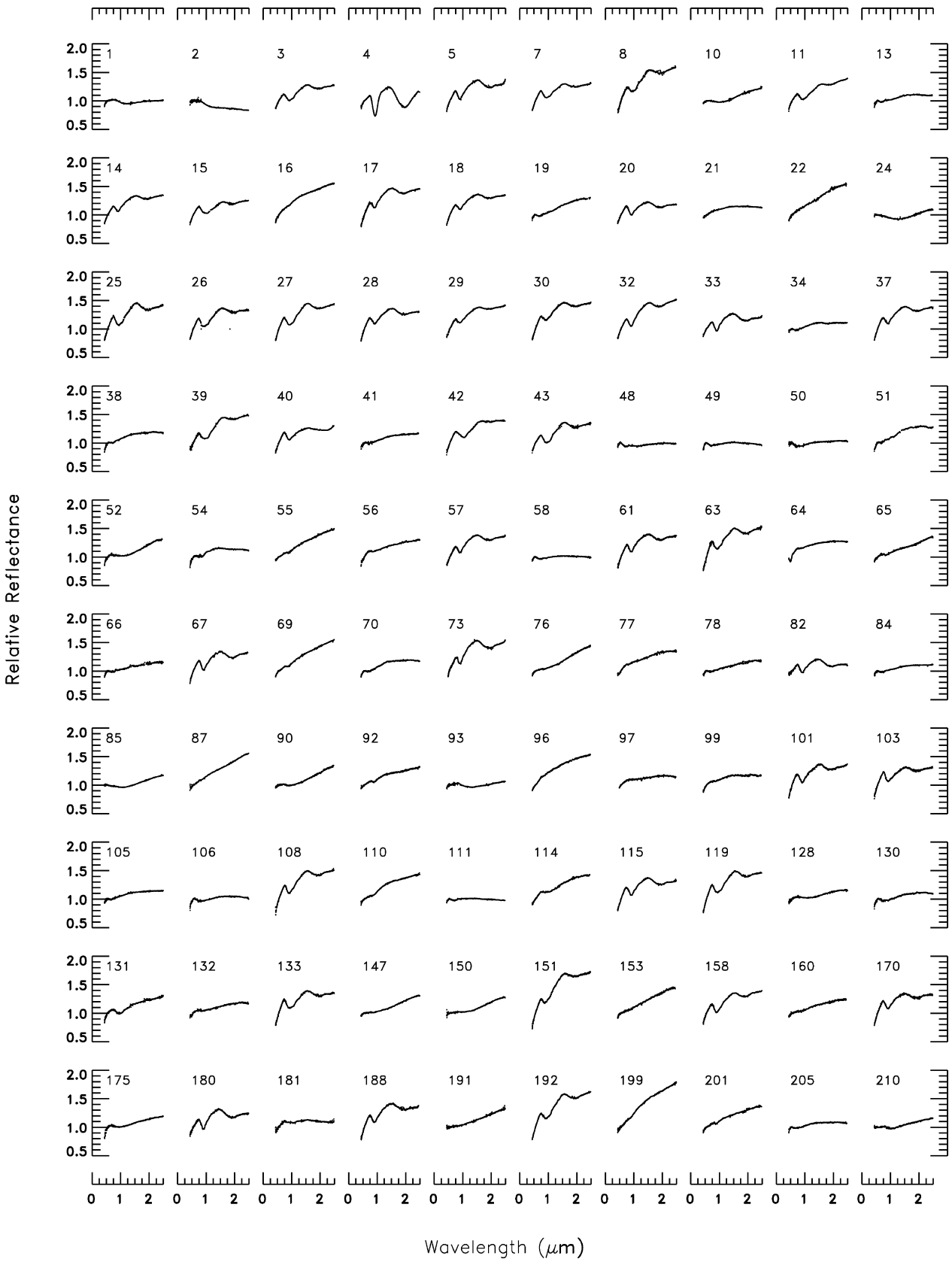

Fig. D. Reflectance spectra for 371 asteroids defining this taxonomy.

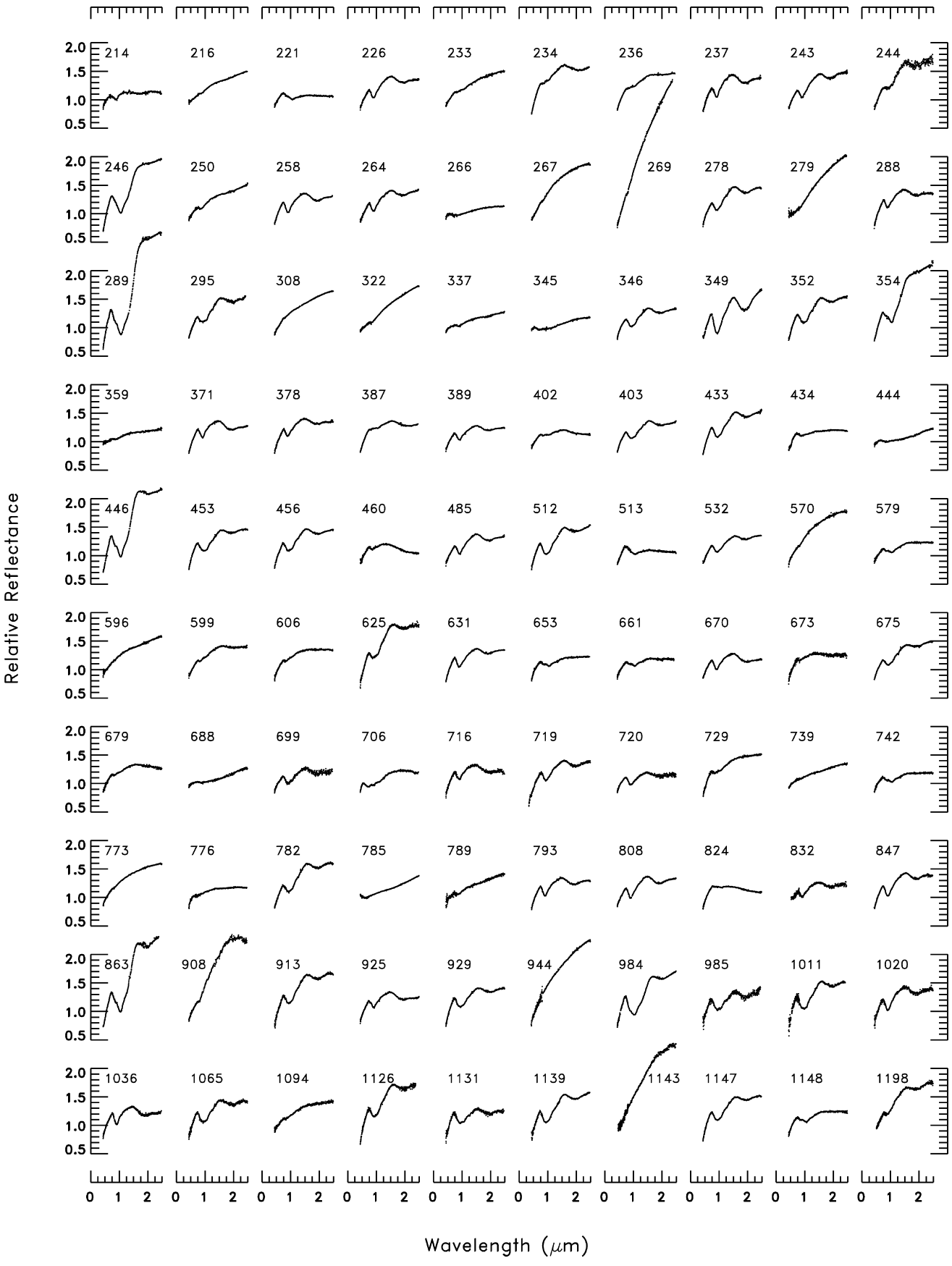

Fig. D. (*continued*)

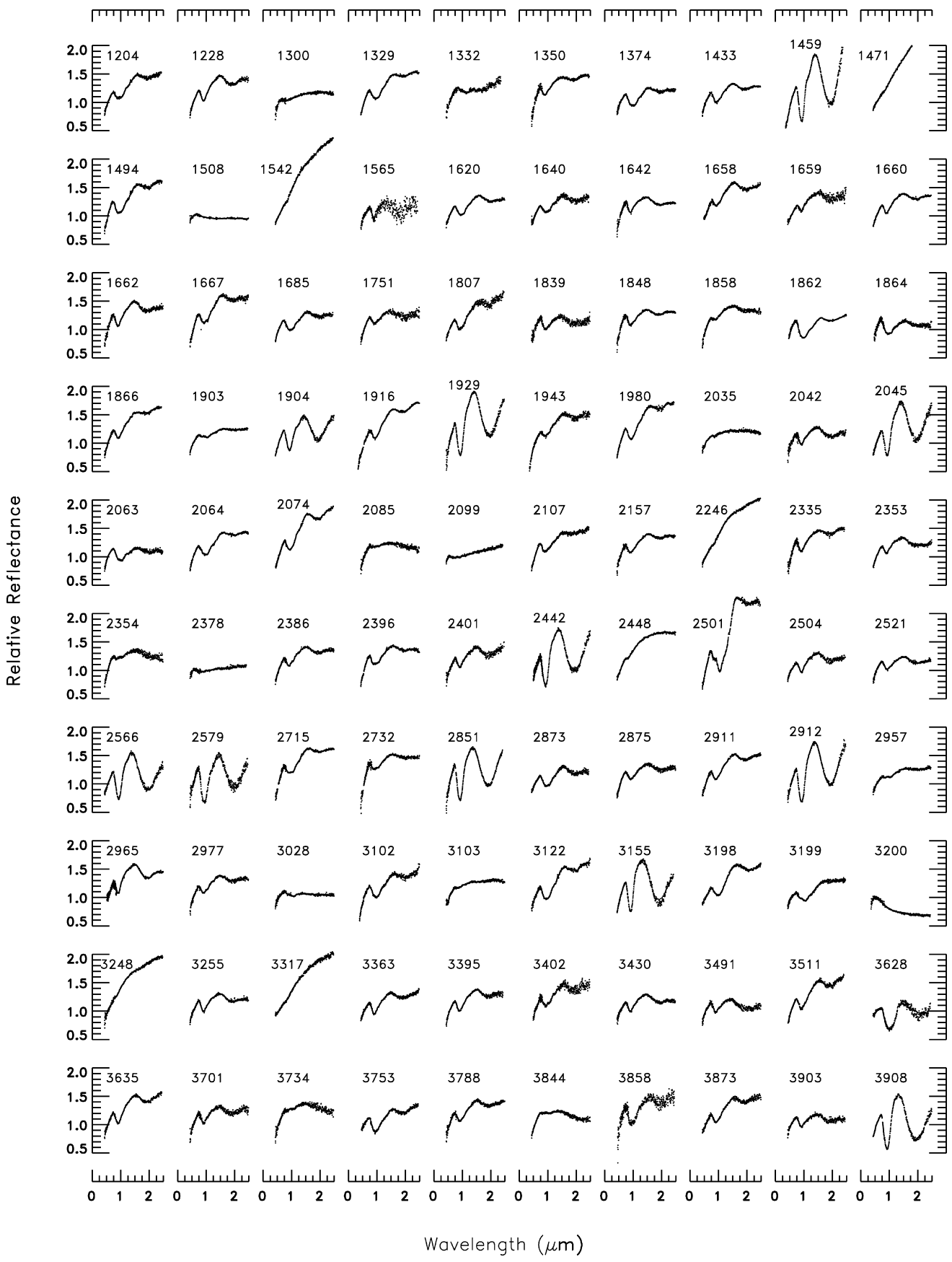

Fig. D. (*continued*)

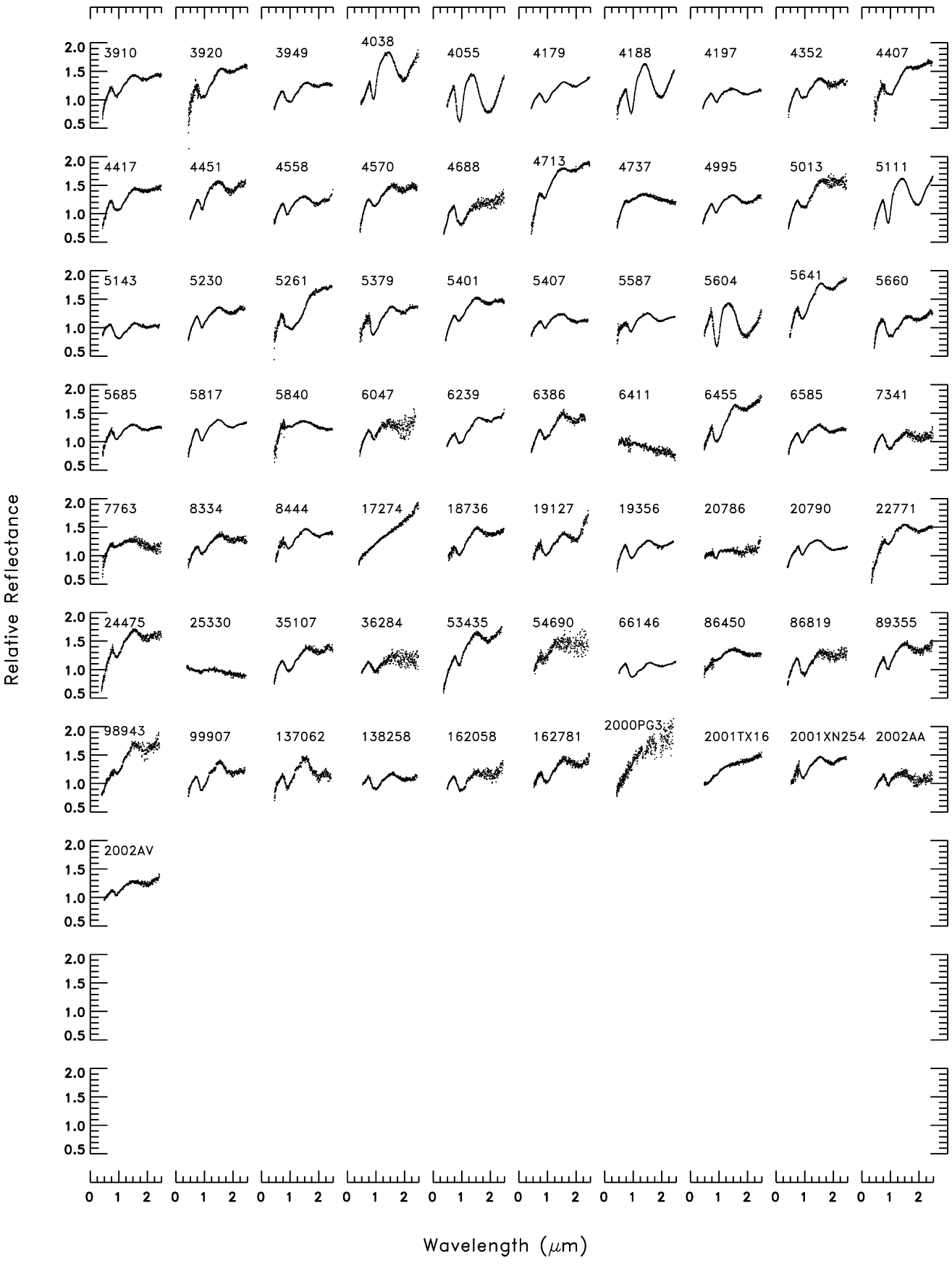

Fig. D. (*continued*)

References

Binzel, R.P., Xu, S., Bus, S.J., Skrutskie, M.F., Meyer, M.R., Knezek, P., Barker, E.S., 1993. Discovery of a main-belt asteroid resembling ordinary chondrite meteorites. Science 262, 1541–1542.

Binzel, R.P., Harris, A.W., Bus, S.J., Burbine, T.H., 2001. Spectral properties of near-Earth objects: Palomar and IRTF results for 48 objects including spacecraft targets (9969) Braille and (10302) 1989 ML. Icarus 151, 139–149.

Binzel, R.P., Birlan, M., Bus, S.J., Harris, A.W., Rivkin, A.S., Fornasier, S., 2004a. Spectral observations for near-Earth objects including potential target 4660 Nereus: Results from Meudon remote observations at the NASA Infrared Telescope Facility (IRTF). Planet. Space Sci. 52, 291–296.

Binzel, R.P., Perozzi, E., Rivkin, A.S., Rossi, A., Harris, A.W., Bus, S.J., Valsecchi, G.B., Slivan, S.M., 2004b. Dynamical and compositional assessment of near-Earth object mission targets. Meteorit. Planet. Sci. 39, 351–366.

Binzel, R.P., Rivkin, A.S., Stuart, J.S., Harris, A.W., Bus, S.J., Burbine, T.H., 2004c. Observed spectral properties of near-Earth objects: Results for population distribution, source regions, and space weathering processes. Icarus 170, 259–294.

Binzel, R.P., Masi, G., Foglia, S., 2006. Prediction and confirmation of V-type asteroids beyond 2.5 AU based on SDSS colors. Bull. Am. Astron. Soc. 38, 627.

Binzel, R.P., Masi, G., Foglia, S., Vernazza, P., Burbine, T.H., Thomas, C.A., Demeo, F.E., Nesvorny, D., Birlan, M., Fulchignoni, M., 2007. Searching for V-type and Q-type main-belt asteroids based on SDSS colors. Lunar Planet. Sci. 38, 1851.

Burbine, T.H., 2000. Forging asteroid–meteorite relationships through reflectance spectroscopy. Ph.D. thesis, Massachusetts Institute of Technology.

Burbine, T.H., Binzel, R.P., 2002. Small main-belt asteroid spectroscopic survey in the near-infrared. Icarus 159, 468–499.

Bus, S.J., 1999. Compositional structure in the asteroid belt: Results of a spectroscopic survey. Ph.D. thesis, Massachusetts Institute of Technology.

Bus, S.J., Binzel, R.P., 2002a. Phase II of the small main-belt asteroid spectroscopic survey, the observations. Icarus 158, 106–145.

Bus, S.J., Binzel, R.P., 2002b. Phase II of the small main-belt asteroid spectroscopic survey, a feature-based taxonomy. Icarus 158, 146–177.

Chapman, C.R., Johnson, T.V., McCord, T.B., 1971. A review of spectrophotometric studies of asteroids. In: Gehrels, T. (Ed.), Physical Studies of Minor Planets. IAU Colloq., vol. 12, pp. 51–65.

Clark, B.E., Hapke, B., Pieters, C., Britt, D., 2002. Asteroid space weathering and regolith evolution. In: Bottke, W.F., Cellino, A., Paolicchi, P. (Eds.), Asteroids III. Univ. of Arizona Press, Tucson, pp. 585–599.

Cohen, M., Walker, R.G., Barlow, M.J., Deacon, J.R., 1992. Spectral irradiance calibration in the infrared. I. Ground-based and IRAS broadband calibrations. Astron. J. 104, 1650–1657.

DeMeo, F., Binzel, R.P., 2008. Comets in the near-Earth object population. Icarus 194, 436–449.

Gaffey, M.J., Burbine, T.H., Piatek, J.L., Reed, K.L., Chaky, D.A., Bell, J.F., Brown, R.H., 1993. Mineralogical variations within the S-type asteroid class. Icarus 106, 573–602.

Howell, E.S., Merenyi, E., Lebofsky, L.A., 1994. Classification of asteroid spectra using a neural network. J. Geophys. Res. 99, 10847–10865.

Lazzaro, D., Michtchenko, T., Carvano, J.M., Binzel, R.P., Bus, S.J., Burbine, T.H., Mothé-Diniz, T., Florczak, M., Angeli, C.A., Harris, A.W., 2000. Discovery of a basaltic asteroid in the outer main belt. Science 288, 2033–2035.

Lord, S.D., 1992. A new software tool for computing earth's atmospheric transmission of near- and far-infrared radiation. NASA Tech. Mem. 103957.

Moskovitz, N.A., Jedicke, R., Gaidos, E., Willman, M., Nesvorny, D., Fevig, R., Ivezic, Z., 2008. The distribution of basaltic asteroids in the main belt. Icarus 198, 77–90.

Rayner, J.T., Toomey, D.W., Onaka, P.M., Denault, A.J., Stahlberger, W.E., Vacca, W.E., Cushing, M.C., Wang, S., 2003. SpeX: A medium-resolution 0.8–5.5 micron spectrograph and imager for the NASA infrared telescope facility. Astron. Soc. Pacific 115, 362–382.

Rivkin, A.S., Binzel, R.P., Bus, S.J., 2005. Constraining near-Earth object albedos using near-infrared spectroscopy. Icarus 175, 175–180.

Tholen, D.J., 1984. Asteroid taxonomy from cluster analysis of photometry. Ph.D. thesis, University of Arizona.

Tody, D., 1993. IRAF in the nineties. In: Hanisch, R.J., Brissenden, R.J.V., Barnes, J. (Eds.), Astronomical Data. Analysis Software and Systems II. In: A.S.P. Conference Ser., vol. 52, p. 173.

Wood, X.H.J., Kuiper, G.P., 1963. Photometric studies of asteroids. Astrophys. J. 137, 1279–1285.

Xu, S., 1994. CCD photometry and spectroscopy of small main-belt asteroids. Ph.D. thesis, Massachusetts Institute of Technology.

Xu, S., Binzel, R.P., Burbine, T.H., Bus, S.J., 1995. Small main-belt asteroid spectroscopic survey: Initial results. Icarus 115, 1–35.

Zellner, B., Tholen, D.J., Tedesco, E.F., 1985. The eight-color asteroid survey: Results for 589 minor planets. Icarus 61, 335–416.